Optogenetic control of pheromone gradients reveals functional limits of mating behavior in budding yeast

Alvaro Banderas[1,*], Maud Hofmann[1], Celine Cordier[1], Matthias Le Bec[1], Carolina Elizondo[1], Lionel Chiron[1], Sylvain Pouzet[1], Vittore Scolari[1,2] and Pascal Hersen[1,*]

[1] *Institut Curie, Université PSL, Sorbonne Université, CNRS UMR168, Physics of Cells and Cancer, 75005 Paris, France.*

[2] *Institut Curie, Université PSL, Sorbonne Université, CNRS UMR3664, Laboratoire Dynamique du Noyau, 75005 Paris, France.*

**Corresponding authors: alvaro.banderas@curie.fr* and *pascal.hersen@curie.fr*

Keywords: Optogenetics, Mating, Budding Yeast, Cell-cell communication, Pheromone, Reaction-Diffusion, Gradients

Abstract

Cell-cell communication through diffusible signals allows distant cells to coordinate biological functions. Such coordination depends on the signal landscapes generated by emitter cells and the sensory capacities of receiver cells. In contrast to morphogen gradients in embryonic development, microbial signal landscapes occur in open space with variable cell densities, spatial distributions, and physical environments. How do microbes shape signal landscapes to communicate robustly under such circumstances remains an unanswered question. Here we combined quantitative spatial optogenetics with biophysical theory to show that in the mating system of budding yeast—

23 where two mates communicate to fuse—signal landscapes convey demographic or positional
24 information depending on the spatial organization of mating populations. This happens because
25 α-factor pheromone and its mate-produced protease Bar1 have characteristic wide and narrow
26 diffusion profiles, respectively. Functionally, MATα populations signal their presence as
27 collectives, but not their position as individuals, and Bar1 is a sink of alpha-factor, capable of both
28 density-dependent global attenuation and local gradient amplification. We anticipate that
29 optogenetic control of signal landscapes will be instrumental to quantitatively understand the
30 spatial behavior of natural and engineered cell-cell communication systems.
31

1. Introduction

Cell-cell communication through extracellular signals enables the spatiotemporal coordination of cell behavior across various scales, from single cells to tissues. The interplay between signal production, diffusion, and reaction (e.g., internalization, adsorption, and degradation) shapes the concentration landscapes that cells experience and ultimately determines a cell's responses. A classic example is the establishment of positional information in the *Drosophila melanogaster* syncytial embryo, in which an exponentially decaying extracellular *bicoid* morphogen gradient forms as a result of the specific location of emitter nuclei on the anterior region, free diffusion of the signal, and homogenous degradation of the signal throughout the embryo[1,2]. This smooth gradient is "read" by nuclei to switch on specific differentiation programs in sharply defined spatial locations.

In contrast to multicellular developmental systems where cells follow a predefined program from a well-defined initial condition, communication does not occur within closed spaces for free-living microbes. Populations of single cells often have a random spatial distribution, expand freely, explore an unknown environment, and create an ecosystem—the size and dynamics of which are the result of cellular metabolic interactions and cell-cell communication. As in development, signal landscapes depend on reaction-diffusion dynamics; however, population-level parameters such as cell density, population composition, and the spatial distribution of emitter and receiver cells are inherently variable in the context of single-cell populations. Thus, the way cells extract information and take appropriate decisions in such an uncertain environment is a very different biological problem than what is observed in embryology.

53 The importance of this question can be epitomized by the commonly accepted view that, in bacteria,
54 communication through diffusible signals provides demographic rather than positional
55 information. The use of demographic information by cells for decision-making is usually termed
56 quorum sensing[3], a mode of communication in which the signal concentration is proportional to
57 the population density, which allows cells—that act both as emitters and receivers—to activate
58 specific phenotypes once a signal threshold is sensed. Crucially, cell spatial organization and signal
59 diffusion (and degradation) in quorum-sensing systems have been experimentally shown to play
60 an important role in how much a cell can perceive the local—rather than the global—population
61 composition through "short-range" communication[4,5]. Short-range communication in bacteria is
62 not argued to provide positional information (position and orientation respect to a source), as
63 bacterial cells are often too small to perceive gradients. Rather, signals reflect the local population
64 composition which informs bacteria about the likelihood of interacting with a relevant partner.

65 In contrast to bacteria, in the well-known example of mating through pheromone communication
66 in the budding yeast *Saccharomyces cerevisiae*, information gathered by cells is usually considered
67 positional, i.e., gradients formed will attract cells to grow towards the position of the source and
68 cells possess mechanisms to perceive the direction of the gradient. Nonetheless, as in bacteria,
69 demographic information has also been shown to be a relevant cue in mating decision making[6]
70 and, furthermore, positional information seems to be available to cells only over very short
71 (contact) distances from partners[7].

However, unlike developmental and bacterial communication, both positional and demographic information are entangled in the case of yeast. How yeast cells perceive demographic and positional information to their benefit remains an unresolved question.

Mating in yeast is governed by the mating-pheromone pathway,[8,9] which relies on the secretion of pheromones to signal the presence of different mating types (*MAT***a** and *MAT*α). The *MAT***a** and *MAT*α mating-types exchange pheromones to trigger activation of their mating pathway, orchestrating a dedicated transcriptional program, cell cycle arrest, and morphological changes that culminate with cell and diploid formation. Distinct branches of the pheromone pathway control transcriptional (Ste2 branch) and arrest/morphology behaviors (Far1 branch). Dose-response experiments measuring the responses of *MAT***a** cells to the purified pheromone α-factor in bulk showed that, while the transcriptional branch of the pathway displays a Michaelian (linear at low doses) input-output relation[10], cells transition sharply—following a Hill-type sigmoidal response—from proliferating to growth-arrested elongated phenotypes, called mating protrusions (or "shmoos")[11,12]. This "mating switch" **(Fig. 1A)** was notably observed in artificial gradients of α-factor[13,14] generated using microfluidic devices. In this setting, cell cycle-arrested morphologies were observed over a narrow range of concentrations (1–5 nM) of α-factor. Cells only displayed chemotropic behavior, elongating their cell body up the α-factor gradient, within this concentration range. However, importantly, it remains unknown how the amplitude and steepness of artificially generated gradients in the context of microfluidic devices compare to the gradients that are generated within heterogeneous, large populations of mating cells.

92 *MAT***a** cells secrete the Bar1 protein which degrades α-factor extracellularly. Thus, the pheromone
93 landscape[6] that *MAT***a** cells experience is not only determined by spatiotemporal diffusion of the
94 α-factor pheromone produced by *MAT*α cells, but also by the concentration of Bar1 they produce
95 themselves.

96 For a non-motile organism such as *S. cerevisiae*, evolution would be expected to produce systems
97 where the concentrations of α-factor that trigger mating are found only in the close vicinity of
98 emitter cells, so that cells do not have mating responses unless they are very close to a partner. Bar1
99 has been deemed responsible to exert such a function[15], by increasing the degradation rate of α-
100 factor and confining its activity close to the producer cells, consequently shortening the length-
101 scale at which mating sensing occurs to only a few micrometers (a fraction of cell size). However,
102 the concentration of Bar1 during mating reactions is dependent on the density of *MAT***a** cells;
103 therefore, the levels of Bar1 may not always be sufficient to degrade the α-factor produced by cells
104 of the opposing mating type. This implies that the mating switch distance can be, in theory,
105 extended further away from the source position (**Fig. 1B**). This scenario is plausible in outcrossing
106 reactions, where a *MAT*α cell within a single mating-type population can switch into a *MAT***a** cell
107 (and vice versa) by means of the *HO* endonuclease activity[16]. Consequently, the superimposition of
108 gradients produced by multiple pheromone sources represents a potential confounding factor (**Fig.**
109 **1C**): partners located at a distance from source cells cannot decide with which partner to mate[17]. To
110 put it differently, it remains unclear how cells extract relevant positional information from
111 physiological pheromone concentration landscapes[6]. Indeed, in mating discrimination assays[17],
112 *bar1Δ MAT***a** can discriminate real emitters from dummy (that do not produce pheromone)

113 emitters, but only if real emitters are in the minority. This suggests that in the absence of
114 degradation, pheromone halos from other cells can be a confounding factor for receiver cells.

115 Several theories have attributed various possible functions to Bar1 in mating populations. Three of
116 these theories depend on high local concentrations of Bar1 in receiver cells, acting as a localized
117 sinks of α-factor: (i) reducing the size of the pheromone halo around emitters (at the expense of
118 gradient strength) to correctly align to gradients in the presence of multiple sources[18], (ii) gradient
119 disentanglement from two sources in close-proximity (intra-ascus) interactions,[19] and (iii) mutual-
120 avoidance in *MAT***a** cells[20]. However, evidence for *MAT***a** receivers acting as pheromone sinks
121 during mating is currently lacking and its quantitative contribution to α-factor gradient reshaping
122 during mating has not been determined.

123 Understanding the spatial properties of α-factor-mediated communication between mating types
124 requires characterizing the properties of physiological α-factor gradients. Although the shape of
125 gradients can be inferred using numerical simulations of cells randomly arranged in space[21], the
126 inability to experimentally control α-factor production locally and the high response variability
127 among receivers preclude the construction of predictive models. To build and test predictive
128 models, one must first obtain quantitative measurements over a large number of cells within large
129 areas in which both mating types are spatially organized. Although possible, the physical
130 separation of mating types in microfluidic devices[22] or by micromanipulation[23] is very tedious to
131 achieve and hard to monitor and reproduce. Thus, while a method to obtain reliable spatial control
132 of α-factor production within physiological range at both large and small scales is critical, no
133 proven method currently exists.

134 Here, we address this problem using the power of optogenetics (**Fig. 1D**). We employed spatial
135 control of α-factor production and degradation in *Saccharomyces cerevisiae* and obtained a
136 quantitative description of extracellular α-factor gradients under physiological conditions.
137 Combined with a diffusion-reaction model, we inferred quantitative parameters that describe the
138 mating communication system and provide a proof of principle for the rational, quantitative
139 control of extracellular signal gradients within microbial cell populations.

140 # 2. Results

141 **2.1 Engineered optogenetic induction of physiological α-factor levels allows spatial control of**
142 **mating.**

143 We first aimed at engineering light-inducible strains that can produce physiological levels of
144 pheromone, by improving on a previous strain design[24]. For this we first engineered wild-type
145 *MAT*α yeast cells using a CRISPR-based promoter replacement strategy (**see Methods**) to replace
146 the promoter of the two α-factor pheromone-coding genes (MF-α1 and MF-α2) with the P_{C120}
147 promoter, the activity of which is induced by the light-sensitive transcriptional activator EL222[25].
148 Additionally, to increase α-factor production and recover wild-type levels, a second copy of the
149 P_{C120}-MFα1 construct was inserted at an unrelated locus (**Fig. 2A, Figure S1, see Methods**) to yield
150 the "opto-α" strain used in this study. To quantify the levels of α-factor produced by the opto-α
151 strain, we used a *MAT***a** reporter strain that harbors a super-folder green fluorescent protein (GFP)
152 downstream of the P_{FUS1} pheromone-responsive promoter[26] (**Fig. 2B**). This reporter strain harbors
153 the native untranslated terminal region (UTR) of FUS1 and carries a ubiquitination sequence that

154 targets super-folder GFP for faster degradation, thus providing a good estimate of the abundance
155 of the native transcript[26]. We stimulated mixes of opto-α and reporter strains with light using a
156 custom-made light-plate apparatus[27] and quantified the levels of the α-factor pheromone (relative
157 to the wild-type MATα strains) using two reporter strains that either carry or lack the Bar1 protease
158 (**Fig. 2B**).

159 In both cases, the levels of α-factor were light-intensity dependent. In the absence of Bar1,
160 pheromone levels comfortably reached the induction levels achieved by the wild type. Under the
161 more stringent conditions where receiver cells express Bar1, the opto-α strain reached up to ~60%
162 of the wild-type response. As other strains and conditions resulted in lower α-factor production
163 levels (**Fig. S1,S2**), we focused on the opto-α strain. Next, we checked if the levels of pheromone
164 produced can rescue wild-type physiological behavior. For this, we tested the capacity of *MAT***a**-
165 *bar1*Δ reporter cells to develop mating protrusions in response to light-induced α-factor production
166 by opto-α cells. With sufficient intensity of light and, like with wild-type *MAT*α emitters, we
167 observed formation of protrusions by *MAT***a** *bar1*Δ cells in gel-embedded mixes (**Fig. 2C, see**
168 **Methods**). Finally, we assayed diploid formation in opto-α/*MAT***a** mixes as a measure of the final
169 physiological output of the mating pathway (**Fig. 2 D,E**). For this, we developed an "optogenetic
170 mating assay" (**Fig. S3, see Methods**) based on three features. First, we used the top-agar technique
171 to embed mating mixtures (as used in classical growth arrest assays), which provides a
172 homogeneous layer where cells are located sparsely and grow as microcolonies. Second, we
173 employed a digital micromirror device (DMD)[28] to expose the cells to spatial light patterns
174 projected into the agar (**See Methods**); and finally, auxotrophic markers were used to ensure that
175 only diploid colonies can grow, allowing us to have a measure of light-induced mating efficiency.

176 Our results show that pheromone production is indeed sufficient to induce cell-cell fusion with
177 wild-type *MAT***a** in a light dose-dependent manner and could reach comparable maximum levels
178 as the wild-type *MAT*α emitter (**Fig. 2 C,D**).

179 Taken together, these results show that the opto-α strain is a suitable candidate, comparable to the
180 wild-type, that produces physiological levels of pheromone production and mating behavior in
181 response to light. Therefore, we employed the opto-α strain as a remotely controlled signal
182 generator to create realistic α-factor spatial gradients within large populations of opto-α/MATa
183 cells.

184 **2.2 Optogenetic induction of pheromone degradation allows specific control of growth.**

185 It is expected that both pheromone production and pheromone degradation by the α-factor
186 protease Bar1 shape extracellular pheromone gradients[21]. To gain spatial control over pheromone
187 degradation, we constructed the opto-Bar1 *MAT***a** strain, in which the α-factor protease Bar1
188 expression is placed under control of the P_{C120} light-inducible promoter. We followed a similar
189 promoter replacement strategy as for the opto-α strain, targeting the Bar1 locus in *MAT***a** cells (**Fig.**
190 **3A**). The expression levels and activity of Bar1 protein were measured using the *MAT***a** *bar1*Δ α-
191 factor reporter, in the presence of purified α-factor added to the media. The levels of GFP produced
192 by the reporter strain were used to quantify the production of Bar1, since Bar1 degrades purified
193 α-factor in the culture medium (**Fig. 3A**). We observed light-dependent Bar1 activity, with the level
194 of the reporter response decreasing as the light intensity increased (**Fig. 3B**). We reached higher
195 Bar1 activity than the wild-type strain and undetectable basal (in the dark) Bar1 enzymatic activity.

196 Although Bar1 degrades the pheromone, its function has been long associated with increases in
197 mating efficiency through several candidate mechanisms[17–20,26] (see **Introduction**). However, the
198 presence of Bar1 is not essential for mating itself. Indeed, when performing the optogenetic mating
199 assay with the opto-Bar1 strain, cells located in dark regions—where *MAT***a** cells do not express
200 Bar1—remain proficient at forming diploids (**Fig. 3C**), with a ~2-fold difference in mating efficiency
201 between illuminated and dark regions (**Fig. S4**). Thus, contrary to optogenetic pheromone
202 induction—and as expected—optogenetic pheromone degradation does not restrict but mildly
203 enhances the final output of the pathway, namely the formation of diploids.

204 Cell cycle arrest, another physiological output of mating events, is controlled by the mating-
205 pheromone pathway through the FAR1 branch[29]. When Bar1 is produced and actively degrades α-
206 factor, one would expect to observe fewer cell cycle arrest events. Following similar methods as for
207 diploid formation, we used the optogenetic plate assay to measure the capacity of *MAT***a** cells to
208 escape cell cycle arrest as a function of Bar1 induction. We imaged an intermediate stage of the
209 experiment (**Fig. 3D**). A differential growth pattern was observed in the non-selective plate used
210 as template for replica plating in diploid-selective media (See also **Fig. S3**), as illuminated cells
211 (expressing Bar1) grew similarly to wild-type levels, whereas non-illuminated cells did not grow
212 significantly (**Fig. 3D-F).**

213 These results show that illuminated opto-bar1 cells recover the expected wild-type behavior in
214 terms of α-factor degradation activity, mating, and proliferation.

215 **2.3 Spatial optogenetic induction of α-factor production generates distance-dependent**
216 **responses in mating populations.**

217 After quantitative characterization of our optogenetic strains, we next moved to assess the spatial
218 properties of pheromone-mediated communication between *MAT*$\boldsymbol{\alpha}$ and *MAT***a** cells in an idealized
219 (but physiological) context. To that end, we implemented the "half-domain assay", which consists
220 of monitoring *MAT*α/*MAT***a** mating reactions within a spatially homogeneous random distribution
221 of cells of both mating types placed at the bottom of agarose-embedded "miniwells" (**Fig. 4A, see**
222 **Methods**). Half of the total surface was exposed to blue light, to optogenetically induce pheromone
223 production exclusively in the illuminated domain. The response of reporter cells in the dark
224 domain allowed us to read and quantify the diffusion-reaction properties of α-factor.

225 We first conducted experiments with the opto-α strain as a light-dependent pheromone generator
226 and the *bar1Δ MAT***a** reporter strain as a pheromone receiver and fluorescent reporter of mating
227 behavior. Absence of Bar1 simulates natural situations where wild-type *MAT***a** receivers are in the
228 minority (e.g., upon a mating type switching event), where Bar1 levels are not enough to modify
229 the global pheromone concentration. Thus, in this experiment, enzymatic degradation of α-factor
230 by Bar1 is absent and disappearance of the pheromone is solely determined by its intake by cells[30].
231 After illumination (**See Methods**), cells along a stripe located in the center of the plate, with its long
232 axis perpendicular to the light-dark interface, were imaged (**Fig. 4B)**. A schematic of the experiment
233 and strains used is also shown (**Fig. 4C**). The opto-α strain was equipped with a red nuclear marker
234 (the HTB2 histone fused to mApple) for easy identification, which is especially important in regions
235 of clumping (**Fig. S5**, this new strain is named opto-α*). We used a 20x objective and an automated
236 stitching method (**see Methods**) to obtain images of a large stripe (5671 μm x 330 μm) of both cell
237 types using fluorescence and bright field microscopy at single-cell resolution (**Fig. S5**). Our
238 experimental results revealed a sharp phenotypic transition between illuminated and non-

239 illuminated areas. The sharpness of this transition (compared to the sharpness of the light border)
240 was assessed by running a parallel experiment in neighboring mini-wells by stimulating a control
241 strain that expresses YFP under the control of an equivalent EL222/P_{C120} light-inducible system. This
242 control serves as a biological spatial imprint of the light-stimulated region, to both locate the
243 position of the border in the sample and determine the sharpness of the light border (**Fig. 4D,E**).
244 The region in the vicinity of the light-to-dark transition border illustrates the overall trend of the
245 mating response in the *MAT***a** *bar1*Δ responder population: the GFP signal gradually vanished in
246 cells further and further away from the frontier in the dark domain (**Fig. 4D**). Importantly, since
247 we imaged cells at single-cell resolution, we clearly observed the cell morphology transitioned from
248 elongated shapes to round as the distance from the light to dark frontier increased (**Fig. 4E**).

249 Our assay demonstrates that optogenetics can be used to produce large-scale population-generated
250 gradients of a pheromone to infer the shape of the pheromone gradient through quantification of
251 gene-expression and cell-morphology outputs (**Figs. 4C,D, S5).**

252 **2.4 Quantitative analysis reveals that population-level pheromone gradients are long-range,**
253 **shallow, and limit morphological transitions to the vicinity of the source.**

254 Using the half-domain assay, we next sought to infer the biophysical properties of the generated
255 gradient. Thus, we constructed a biophysical model based on reaction-diffusion dynamics—as well
256 as dose-response functions—and obtained single-cell quantifications of pheromone-responses
257 using a combination of manual and automated single-cell segmentation and analysis (**see**
258 **Methods**). To determine the relevant diffusion-reaction parameters governing pheromone
259 communication between cells, we modeled the steady-state pheromone gradient profiles and the

corresponding induced cell responses. Taking advantage of the symmetry within our experimental setting, we simplified the reaction-diffusion equations to describe a one-dimensional infinite field of pheromone producers (**Fig. 5A**).

$$\frac{\partial c(x,t)}{\partial t} = \mathrm{D}\nabla^2 c(x,t) - \Omega\, \mathrm{c(x,t)} + \rho \mathrm{A}(x), \tag{1}$$

where $c(x,t)$ is the concentration of α-factor, D is its diffusion coefficient, A is the pheromone production rate, ρ is the cell density, and Ω is the rate of degradation of the pheromone by cell uptake[30]. This equation produces the well-known solution for the diffusion equation for a point source under uniform degradation at the steady state, $c^*(x) = \frac{\mathrm{A}}{2\sqrt{\mathrm{D}\Omega}} \mathrm{e}^{-\sqrt{\Omega/\mathrm{D}}\, x}$, which describes gradients formed by a single cell in one dimension. For the half-domain where cells are illuminated and therefore producing pheromone ($x < 0$), the solution depends on the cell density (**Fig. 5B)** and the steady-state pheromone concentration profile is described as follows (see full derivation in **Supplementary Information, Section II**):

$$c(x,\infty) = \begin{cases} \frac{\rho \mathrm{A}}{\Omega} \frac{1}{2} \mathrm{e}^{-\sqrt{\Omega/\mathrm{D}}\, x} & \text{for } x \geq 0, \\ \frac{\rho \mathrm{A}}{\Omega} \left(1 - \frac{1}{2} \mathrm{e}^{\sqrt{\Omega/\mathrm{D}}\, x}\right) & \text{for } x < 0. \end{cases} \tag{2}$$

From this set of equations, we can see that the concentration c at the border ($x = 0$) is greater for the half-domain production compared to a single point-source only for the condition where the density of producers is greater than one point-source within one decay length, $\rho > \sqrt{\Omega/\mathrm{D}}$. In other

words, only if the pheromone diffuses far enough, so that the contributions to the gradient from each single cell overlap.

Further, the response $\theta(x,\infty)$ of the mating pheromone pathway to the steady-state concentration of pheromone can be modeled with a Hill function. By composing equation (2) with a Hill function with coefficient n results in:

$$\theta(x,\infty) = \begin{cases} \dfrac{1}{1+\left(C\frac{1}{2}\mathrm{e}^{-\sqrt{\frac{\Omega}{\mathrm{D}}}x}\right)^{-n}} & \text{for } x > 0, \\ \dfrac{1}{1+\left[C\left(1-\frac{1}{2}\mathrm{e}^{\sqrt{\frac{\Omega}{\mathrm{D}}}x}\right)\right]^{-n}} & \text{for } x < 0, \end{cases} \tag{3}$$

where $C \equiv \frac{\rho \mathrm{A}}{\Omega\,\mathrm{EC}_{50}}$ is the concentration of the ligand far away from the border ($x \to -\infty$) in "EC_{50}" units, namely, the concentration producing the half-maximal $\mathrm{P}_{\mathrm{fus1}}$ mediated gene-expression response.

Experimental responses are measured in unknown concentration units, for this reason they have been converted to normalized values by baseline-subtracting and normalizing them to their maximum level before fitting the model (**see Methods**). Equivalently then, equation (3) was normalized by its maximal value $\hat{\theta}(x,\infty) = \theta(x,\infty)/\frac{C^n}{1+C^n}$. This step is fundamental as the non-normalized Hill-equation only saturates at very large concentrations ($C \gg \mathrm{EC}_{50}$), while in all our experiments we determined C (the pheromone concentration at the curve's plateau) to be of the same order of magnitude as its EC_{50} (see below), *i.e.* the response curve becomes flat far from the

295 border in the left domain because of a constant concentration of pheromone, and not because of
296 saturation. Using this approach, we obtained the theoretical shape for a standard concentration
297 profile at various values of C and two different values of n **(Fig. 5C,D)**. It is well known that no
298 cooperativity is involved in the gene expression output from the P_{FUS1} promoter[26], we thus fixed
299 $n = 1$ for gene expression output.

300 Armed with this model, we next quantified the single-cell outputs of the activity of the mating
301 pheromone pathway—specifically, cell elongation (**Fig. 5E**; determined manually; **see Methods**)
302 and P_{FUS1} dependent gene-expression (**Fig. 5F**; determined independently using standard
303 illumination correction and segmentation tools; **see Methods**)—in *MAT***a** cells lacking Bar1. Our
304 results revealed a gradient of fluorescence intensity that extends far beyond the region where the
305 pheromone is generated (**Fig. 5E**). Thus, the transport properties of α-factor can generate responses
306 at distances spanning hundreds of cell lengths, consistent with a widely diffusible molecule. The
307 morphological transition (**Figs. 5F**) is steeper than the gene expression response, with cells
308 increasing their maximal length within a narrower distance range and at a higher pheromone
309 concentration. This is expected, as the morphological transition is indeed switch-like[10,12].

310 We ran control experiments using (i) opto-α emitters mixed with the wild-type *MAT***a** reporter
311 (expressing Bar1) and (ii) a mixture of the wild-type *MAT*α as light-independent emitters and the
312 *MAT***a** *bar1Δ* reporter. To ease cell segmentation, we performed a machine-learning based protocol
313 (See methods) to obtain a global picture of the behavior of both samples and controls. In the reaction
314 with wild-type expression of Bar1, basal GFP output was obtained with no detectable differences
315 between the light and the dark domains. In contrast, in the mix with wild-type *MAT*α and the

316 *MAT***a** *bar1Δ* reporter, strong activation was observed in both illuminated and dark domains (**Fig.**
317 **S6**). These controls further allowed us to compare the maximum GFP output activation of the opto-
318 α and wild-type *MAT*α strains to confirm that the emission levels are close to physiological in the
319 half-domain assay, as well as allowing us to correct illumination inhomogeneities and background-
320 bleaching effects of light induction with an independent method (**Fig. S6, see Methods**).

321 We also observed that cells elongate, but do not preferentially grow towards (nor away from) the
322 large-scale gradient, as revealed by the lack of enrichment of cells with orientations close to 0° or
323 180° respect to the direction of the gradient (**Fig. S7**), demonstrating that—even at its steepest point
324 (the border)—the large-scale gradient is insufficient to induce chemotropism.

325 Next, we assessed the stability of the responses over time to check the adequacy of using a steady-
326 state approximation. We observed that outputs measured in overnight stimulations exhibited a
327 distance-dependent relationship that was equivalent to the same output measured after 5 hours,
328 indicating the shape of the gradient is not dramatically altered at later timepoints (**Fig. S8**).
329 Contrary to that, if no steady state was reached, the gradient would smooth out over time due to
330 accumulation of the pheromone in the dark domain. In addition, because we did not observe
331 formation of single or multiple "thin protrusions", characteristic of saturation of the pheromone
332 pathway[11,31], we concluded that cell responses lie within the sensitive range of the pathway, which
333 is indicative of the Ste2 receptor not being saturated. This further supports the idea that a steady
334 state is reached, because otherwise the pheromone would continue accumulating to reach
335 saturation, at least in its production domain.

336 Next, we used the biophysical model (**see Supplementary information**) to infer key quantitative
337 parameters of the gradient. We fitted the baseline-subtracted, normalized-to-maximum
338 experimental datapoints for the two observables to $\hat{\theta}(x, \infty)$ (**Fig. S9**), with n fixed to one for the
339 gene expression output (**see Methods**). For completeness of information, the fits are displayed on
340 top of the raw data (**Fig. 5E,F**). In this way, we inferred the basic properties of the gradients
341 generated (**Fig. 5G**): the steady-state decay length $\lambda \equiv \sqrt{\frac{\mathrm{D}}{\Omega}} \sim 600$ μm, the steady state concentration
342 of α-factor for $x \ll -\lambda$, $C = 1.6\ \mathrm{EC}_{50}$, and the Hill coefficient of the morphological response ($n = 3$).
343 The gradient value at light-dark transition border, the expected steepest point of the large-scale
344 gradient, has a value of ~1.2 EC_{50} / mm. Using an EC_{50} value for the response of 1–3 nM[10,11,26], we
345 obtain a value of 1.5 to 4.5 pM/μm or, roughly, ~20 pM per cell diameter (one cell diameter is ~5μm).
346 Such shallow gradients will produce differences in receptor occupancy between each side of the
347 cell an order of magnitude below the minimal ~0.5% observed in chemotropic cells in artificial
348 pheromone gradients[32].

349 Collectively, these results imply—in this spatial arrangement and in the absence of Bar1—that: *(i)*
350 pheromone levels characteristically decay roughly ~100 cell bodies away from producer regions or
351 single cells; *(ii)* that maximal steady-state pheromone levels found in typical (dense but not
352 crowded) mating populations are not saturating and rather very similar (less than double) to the
353 EC_{50} of the response (its most sensitive point); *(iii)* that cells "ignore" (filter out) large-scale
354 gradients (such as those produced within the spatial limit of finite emitter populations) that are
355 non-informative about the location of nearby emitters; and *(iv)* although the decay length of the
356 gradient is the same for the half-domain and a single cell (in one dimension), because the linear

357 density is ~100 cells/mm (~60 cells in one decay length), $C/2$ (equivalent to the pheromone levels at
358 the point source) would be reduced by around two orders of magnitude for a single cell. This means
359 that for a single cell, pheromone levels close to the EC_{50} cannot be reached, even in its immediate
360 vicinity. This is consistent with the need for close-proximity mechanisms and focal pheromone
361 emission[7] for such close-contact situations. In other words, single emitters cannot induce elongation
362 or chemotropism in responding cells, even in the absence of Bar1. Sufficient pheromone levels to
363 induce mating behavior at a distance are always produced by a collective of cells and under low
364 Bar1 conditions (biased ratios). Increased rates of degradation of the pheromone (e.g., in the
365 presence of Bar1) would scale down the gradient (See equation (3) in **Supplementary Information**
366 **section II**). These constraints over the maximum levels of pheromone that a single cell can produce
367 might explain why—when homogeneous Bar1 sources are present—we did not observe elongation
368 in either of the two domains (**Fig. S6**) and the response values stayed at basal levels, despite the
369 high density of emitters.

370 **2.5 Quantitative analysis of large-scale gradients produced by opto-Bar1 receivers reveals**
371 **localization of Bar1 activity in its production domain.**

372 Our experiments in the absence of Bar1 are adequate to explain natural situations where wild-type
373 *MAT***a** receivers are in the minority (e.g., upon a mating type switching event), such that Bar1 is not
374 abundant enough to modify the large-scale pheromone landscape. As the mating-type ratio
375 becomes unbiased, *MAT***a**-produced Bar1 protease becomes important. When mated under
376 conditions of pure diffusion-reaction—but not advection—Bar1 is believed to allow reshaping of
377 the pheromone landscape. The exact nature and biological function of this reshaping activity

during mating remains controversial[6]. Therefore, we used the half-domain assay with the opto-Bar1 strain in the presence of wild-type MATα cells as emitters to shed light on the problem.

In this case, WT pheromone production is homogeneously distributed and emission of Bar1 is localized in one half-domain (**Fig. 6A**), on the right of the light-dark transition border (**Fig. 6A, Fig. S10**). For this assay, wild-type *MAT*α emitter cells were tagged with a green nuclear tag, while opto-Bar1 cells were tagged with a red nuclear tag. This allowed us to confirm that, as in the Petri dish experiments (**Fig. 3D-F**, **Fig. S4**), mating events (measured as nuclei fusion events) happen in both illuminated and non-illuminated areas and that Bar1-mediated increases in mating events correlate with the increased initial growth of *MAT***a** (**Fig. S11**). Crucially, observations of the cell-elongation phenotype revealed a striking difference compared to this response's profile in the opto-α experiment (**Fig. 5)**: in the opto-Bar1 case, the elongation pattern emerges far away from the border, well into the dark (left) region of the experiment (**Fig. 6B-C**).

To understand which properties of Bar1 activity and diffusion would yield such a pheromone profile, we explicitly modeled the contribution of Bar1 to the formation of the gradient profile (**Supplementary Information, section III**). In this model, both α-factor and Bar1 diffuse, are produced (in a spatially dependent manner for Bar1) and degrade. These are captured by the two sets of parameters $(\mathrm{D}_\alpha, \mathrm{A}_\alpha, \Omega_\alpha)$ and $(\mathrm{D}_\beta, \mathrm{A}_\beta, \Omega_\beta)$. The enzymatic reaction between Bar1 and α-factor is modelled through a Michaelis-Menten coupling term that contributes to α-factor degradation:

$$\frac{\partial c_\alpha}{\partial t} = \mathrm{D}_\alpha \nabla^2 c_\alpha - \Omega_\alpha c_\alpha - \frac{V_m}{K_M + c_\alpha} c_\beta \cdot c_\alpha + \rho \mathrm{A}_\alpha, \quad \text{and} \quad \frac{\partial c_\beta}{\partial t} = \mathrm{D}_\beta \nabla^2 c_\beta - \Omega_\beta c_\beta + \rho \mathrm{A}_\beta(\mathrm{x}). \qquad (4)$$

Focusing on the second of the two differential equations and considering production in the right half-domain, the Bar1 spatial profile follows a similar pattern as the α-factor spatial profile in the opto-α experiment. Furthermore, knowing the asymptotic limits for $c_\alpha(x)$ (See **Supplementary Information, Section III**), it is then straightforward to numerically solve equation Eq. (4). Importantly, many parameters in Eq. (4) are redundant. Further, Eq. (4) can be simplified by assuming low α-factor concentrations ($c_\alpha < K_M$) reducing the number of parameters to a more meaningful subset. This is justified as the K_M of Bar1 is 30 μM[29], whereas the concentrations of pheromone in our experiment are estimated to be in the nM range, as shown by the opto-α experiment.

Thus, we derive four independent dimensional parameters that fully characterize the solution: the decay lengths of α-factor and Bar1 $\lambda_\alpha = \sqrt{\mathrm{D}_\alpha/\Omega_\alpha}$ and $\lambda_\beta = \sqrt{\mathrm{D}_\beta/\Omega_\beta}$, and the asymptotic constant concentrations of α-factor in the Bar1-free and Bar1-producing domains, $c_\alpha^{max} = \frac{\rho \mathrm{A}_\alpha}{\Omega_\alpha}$ and $c_\alpha^{min} = \frac{1}{1+\frac{1}{K_M}\frac{V_m}{\Omega_\alpha}\frac{\rho \mathrm{A}_\beta}{\Omega_\beta}} \cdot c_\alpha^{max}$. The steady state solution is then composed with the Hill function with coefficient $n = 3$ that yields the elongation response (as in the opto-α experiment), predicting the experimental response curves. Importantly, we measure the c_α^{max} parameter by comparing the morphological response in the opto-Bar1 experiment (**Fig. 6C**) to the one in the opto-α experiment (**Fig 5F)**. This is possible since we reach a constant c_α^{max} in our experiments and this value does not depend on any Bar1 parameters according to the theory. By this simple comparison we obtain a lower maximum pheromone level in the opto-Bar1 experiment than in the opto-α experiment, namely $c_\alpha^{max} = 1.20\ \mathrm{EC}_{50}$. This is obtained by taking the fitted value in the opto-α experiment as a reference and considering the Hill coefficient $n = 3$ in the calculation (**see Methods**).

418 From theory, for any fixed c_α^{max}, it is then possible to determine the location of the half-maximal
419 normalized response λ_0, in λ_α units, as a function of two adimensional parameters: a measure of
420 Bar1 activity c_α^{min} / c_α^{max} and a measure of Bar1 diffusion $\lambda_\beta/\lambda_\alpha$. Larger values of Bar1 diffusion
421 bring the half maximal response to lower negative values (towards the left side) and, similarly,
422 large values of Bar1 activity can do the same. Then, for each precise location of the half maximal
423 response we identified a curve of possible parameters in the (c_α^{min} / c_α^{max}, $\lambda_\beta/\lambda_\alpha$) plane (**Fig 6D, see**
424 **Methods**). Consistent with intuition, the plot shows a clear trade-off between the diffusion and
425 activity of Bar1. Namely, to obtain an equivalent shift, Bar1 with high activity needs to diffuse
426 narrowly, whereas Bar1 with weak activity needs to diffuse widely. To mirror the opto-α
427 experiment and find the distance at which the half-maximal response occurs, we fitted a shifted
428 logistic function with the same steepness n/λ_α obtained in the opto-α experiment fit, leaving the
429 shift as the only free parameter (**Fig 6C**, **see Methods**). The fit gives us a value of $\lambda_0 = -1.16\,\lambda_\alpha$ for
430 the half maximal response location (red line in **Fig. 6C,** corresponding to the red line in **Fig. 6D**).

431 Calculating the diffusion coefficients of Bar1 and α-factor using the Stokes-Einstein equation results
432 in diffusion rates of 104 $\mu m^2/s$ and 361 $\mu m^2/s$, respectively[21]. Thus, in theory, Bar1 diffuses about
433 3.5-fold slower than the pheromone (**Fig 6D**) (assuming similar degradation rates for both). This
434 value corresponds to a value of c_α^{min} / c_α^{max} of 1/10 to 1/20. We then compared this expected result
435 to known measures of Bar1 activity to then estimate the protease's effective diffusion. For this we
436 made an estimation based on pure α-factor dose-response experiments where we identified the
437 growth arrest switch, comparing *MAT***a** wild type and its corresponding Bar1 knockout at an
438 equivalent cell density as in the half-domain assay (**Fig. S12**). Our estimate tells us that, under these

439 conditions, Bar1 reduces the levels of pheromone by at least ~100-fold, displacing the arrest switch
440 from its position which lies very close to the Ste2 receptor Kd (**Fig. S12**). According to our theory
441 (**Fig. 6C**), the ratio of the expected decay lengths for α-factor and Bar1 is $\frac{\lambda_\alpha}{\lambda_\beta}\sim 0.1$. This means that,
442 at the very least, Bar1 diffusion is 10-fold slower than pheromone diffusion (assuming equal
443 degradation rates for both). Thus, we conclude from this experiment that Bar1 tends to stay in its
444 production domain through mechanisms altering diffusion during mating, in contrast to α-factor,
445 which diffuses widely.

446 # 3. Discussion

447 Here, we constructed yeast strains in which pheromone production and degradation can be
448 controlled via optogenetics to shape extracellular signal gradients and thereby provide a better
449 understanding of the functions of cell-cell communication in open space. Using this method, we
450 show that the pheromone landscapes in sparse yeast populations are shaped by a "global excitation
451 - local degradation" process, where α-factor functions as global excitatory signal: biologically
452 relevant concentrations of this pheromone are built up by the contributions of many emitter cells
453 and receiver cells act as sinks for this signal.

454 We demonstrate that there is a relevant length-scale for gradient formation other than that in the
455 immediate vicinity of cells (1 cell body or ~5 μm); namely, the large-scale gradient formed at the
456 edge of finite producer populations. However, these large-scale gradients are not steep enough to
457 induce chemotropism (despite pheromone concentrations being high enough to trigger
458 elongation). Indeed, gradient values capable of inducing chemotropic behavior in the literature are

459 generally steep[7,13,14,33,34]. Chemotropism directed along large-scale gradients was not observed in
460 our half-domain assays. Thus, *MAT*a cells filter out large-scale gradients while, presumably,
461 tracking local small-scale gradients, given the local gradients possess sufficient steepness. Our
462 model allowed us to infer that the concentrations of pheromone emanating from single emitters
463 must be well below the mating threshold (**Fig 5H**), this means that pheromone secretion by single
464 cells cannot not provide positional information, because responders are not sensitive enough to
465 activate chemotropism (**Fig. 6E**)—even sensitized if partners are sensitized (without expressing
466 Bar1).

467 Our results also show that Bar1 diffuses at least 10-fold slower than the pheromone it degrades (**Fig**
468 **6D,F**). Such limited diffusion of Bar1 does not prevent *MAT***a** from modifying global pheromone
469 profiles—provided cells are at a sufficient cell density. Indeed, in our opto-Bar1 experiment (**Fig.**
470 **6A-C**), Bar1 greatly reduces the global α-factor concentration, and *MAT***a** cells do not elongate nor
471 arrest (**Fig S6**). Despite this, cells in close contact still mate normally (**Fig. S11**). Thus, when
472 separated in space, cells cannot reach the threshold for executing the morphological transition. This
473 is in agreement with the absence of elongation and the persistence of cell division by *MAT***a** cells in
474 unbiased mating reactions in the presence of advection[35]. In this sub-threshold case, it is likely that
475 increased cell-number, randomly oriented bipolar budding[35,36] and close-contact mechanisms[7,37] aid
476 mating (**Fig. 6G**). These known mechanisms are functionally very different as search strategies to
477 chemotropism, a function first inferred from the classical experiments by Segall in the early 1990s[34],
478 in which cell-cycle arrested cells in agarose extend their cell bodies towards a glass pipet that
479 releases pheromone. This type of chemotropism, involving cell elongation and cell-cycle arrest, is
480 only accurate at concentrations matching those at which cells switch[38–41]. Therefore, gradients need

481 to fulfill two conditions to induce this behavior: they must have a high mean pheromone
482 concentration to induce elongation and need to be steep enough to direct the polarisome towards
483 the source. Our results suggest that—in mating reactions with cell densities that would render
484 chemotropic cell elongation useful—there is a trade-off between the mean pheromone
485 concentration and the steepness of the gradient: cells are weak producers but, in principle, good
486 position signalers, whereas dense populations are strong signalers but weak position signalers.
487 Thus, our results explain why elongated *MAT***a** chemotropism is rarely observed as directed mate-
488 searching in mating reactions with sparse populations. Indeed, depending on the levels of Bar1,
489 within environments crowded with α-factor emitters, cells will either restrict pheromone levels to
490 the emitter vicinity and rely on local mechanisms[7,37] or exhibit random elongation due to gradient
491 overlapping (**Fig. 6H**). Random cell elongation could be a useful strategy under such low Bar1
492 conditions, as gradient overlapping will make the switch concentration proportional to the cell
493 density of partners, rather than their distances. Our results reveal that gradient overlapping is
494 significant in the absence of Bar1, implying that distance-to-source measurements by cells in the
495 production region cannot be disentangled from demographic measurements**.** Therefore, our results
496 highlight a limitation of chemotropism as an efficient mate-directed search strategy; namely, the
497 necessity of the *MAT*α-biased ratios for *MAT***a** to reach its switching threshold entails an increased
498 likelihood of producing local, uninformative gradients caused by increased overlapping. This
499 trade-off, in principle, could be balanced at some specific ratio, where Bar1 levels are enough to
500 spatially restrict levels of α-factor and sources are clustered to allow a high local concentration of
501 α-factor. This could be the case, for example, for a large microcolony of MATα encountering a close

502 smaller microcolony of *MAT***a** (e.g., microcolony growth after mating type switching events or
503 spore dispersal[42,43]).

504 Rappaport and Barkai[19] defined a theory for Bar1 as a perfect (or nearly perfect) α-factor sink where
505 most α-factor molecules that impinge upon *MAT***a** cells are absorbed, rather than released back into
506 the medium. This process—Bar1 dependent degradation—contrary to other mechanisms, such as
507 receptor endocytosis-mediated internalization, allows both absorption at the cell surface and
508 degradation in the media. In our experiments, when gradients were formed by the pheromone-
509 degrading enzyme Bar1 secreted by *MAT***a** under uniform α-factor production throughout space,
510 the response patterns revealed that the extent of Bar1 diffusion during the timescales relevant for
511 mating are very low. The evidence for Bar1 being a widely diffusible protein came from an early
512 study by Hicks and Herkowitz[23], who developed the "N-assay" in which α-factor gradients are
513 generated in agar with a heavy streak of *MAT*α cells and "tester" *MAT***a** cells are micromanipulated
514 and placed at different distances from the source to estimate the concentration of α-factor. When
515 the assay is performed on agar where a heavy streak of wild-type *MAT***a** (producing Bar1) was
516 allowed to stay on the opposite side of the agar for six hours and then cut out, the levels of
517 stimulation reduced compared to the fresh, untreated agar. Several possibilities could explain this
518 inconsistency. First, in the assay by Hicks and Herkowitz, Bar1 may have diffused poorly, staying
519 in the region close to the cut fraction, but reshaped α-factor gradients by providing a sink region—
520 similarly to our experiment. Second, because our assay retains physiological conditions both in and
521 out of the Bar1 production half-domain, the cell density of both emitters and receivers is high
522 (unlike in the "N-assay"). Therefore, cells could effectively lower Bar1 mobility by providing an
523 adsorption surface based on cell-wall mannan interactions. Indeed, Bar1 is an abundant disulfide-

524 bridged mannoprotein present in the cell wall of *MAT***a** cells[44] and this sink character is essential to
525 build models that explain the establishment of gradient disentanglement from two sources in close-
526 proximity intra-ascus interactions[19] and mutual-avoidance in *MAT***a** cells[20]. The latter of these
527 mechanisms is relevant to germinating spores during outcrossing in ecologically realistic
528 scenarios[43,45] and requires similar conditions as in our experiment. The cell wall-associated fraction
529 of Bar1 allows it to work as a sink for α-factor while retaining the capacity of the enzyme to diffuse.

530 Overall, our results suggest that the pheromone landscapes in "open" mating reactions are directly
531 shaped by population parameters and differential diffusion of Bar1 and α-factor. Functionally,
532 steep gradients localized at either the source or the sink can only guide chemotropism when the
533 population ratios are biased enough to limit global Bar1 availability. Due to its sink function, the
534 gradients might be steeper at a receiver cell; thus, if several receiver cells cluster, the gradients can
535 direct these cells away from each other[20]. Thus, gradients can effectively provide information about
536 the location of competitors (other *MAT***a** cells) rather than potential mates (*MAT*α cells). In addition,
537 local degradation of α-factor allows the asexual proliferation of unmated individuals, maximizing
538 the total population's fitness.

539 Our results open the door for creating more complex spatial patterns and the dynamic control of
540 pheromone production and degradation simultaneously, by diversifying the types of optogenetic
541 control possible. Such complexification will allow to simulate natural situations—e.g., optogenetic
542 induction of mating type switching—and to create synthetic communication landscapes with
543 useful applications in engineered living materials. Our study encourages the use of the yeast

544 mating system as a quantitative framework for the design and control of spatial behavior of natural
545 and synthetic cell-cell communication systems.

546 4. Methods

547 All materials described here and in the Supplementary Information are available upon reasonable
548 request. Datasets used to generate the figures and the code for the mathematical modelling can be
549 found on the public Zenodo archive 10.5281/zenodo.10572403

550 4.1 Strains and growth conditions

551 *S. cerevisiae* strains used in this study (**Supplementary Table 1**) are derivatives of BY4741 (*MAT***a**
552 *his3Δ1 leu2Δ0 met15Δ0*), BY4742 (MATα, *lys2Δ0,* otherwise identical to BY4741), SEY6210a[46] (*MAT***a**
553 *leu2-3,112 ura3-52 his3Δ200 trp1Δ901 lys2-801 suc2Δ9*), and SEY6210 (MATα, otherwise identical to
554 SEY6210a). Yeast cells were routinely grown on complete medium (Yeast peptone dextrose; YPD,
555 Sigma) or synthetic complete (SC) medium—composed of 6.7 g Yeast Nitrogen Base without amino
556 acids (Difco 291940) and 0.8 g complete supplement mixture drop-out (Formedium DCS0019) in 1
557 L—supplemented with 2% glucose (Merck). Cells from glycerol stocks or agar plates were
558 inoculated into YPD and incubated at 30°C on an orbital shaker at 250 rpm (in an Innova 4230
559 incubator) for 12 to 16 h. Day cultures were performed by inoculating 5 mL of SC or YPD media
560 with overnight cultures at a concentration of 1% *v*/*v*. Care was taken to reduce unwanted light
561 exposure as much as possible before the start of the experiments by covering the agar plates and
562 precultures in aluminum foil and by performing all steps without direct exposure to light (low
563 ambient light).

564 All yeast transformations were conducted following a standard lithium acetate protocol. To replace
565 the native promoters located upstream of the genes of interest with the EL222-dependent promoter
566 P_{C120}, we performed CRISPR/Cas9-based genome editing following a method described
567 previously[47]. Oligonucleotides used in this study are listed in **Supplementary Table 2**. The
568 replacement fragments used to exchange the upstream region of the relevant genes (pheromones
569 or Bar1) were amplified from plasmid pYTK097, which contains the original sequence of the wild-
570 type P_{C120} promoter from *Erythrobacter litoralis*[48], using primers containing appropriate homology
571 regions as overhangs. DNA sequences coding for guide-RNA (gRNA) sequences (obtained from
572 IDT) used to target Cas9 to the desired loci are also listed in **Supplementary Table 2**. Short and
573 long gRNA were hybridized with each other and ligated into plasmid pML104, which possesses a
574 *Cas9* expression cassette and an URA3 marker for auxotrophic selection. The EL222 transcription
575 factor was inserted at the HIS3 locus by digesting plasmid pEZ-L105[49] with the *SfiI* restriction
576 enzyme. In this construct, EL222 is expressed from the constitutive P_{pgk1} promoter. Nuclear tagging
577 was performed by inserting mApple at the HTB2 locus by amplifying mApple from plasmid
578 pPH330 using primers oPH_0386 and oPH_0387 followed by transformation and selection using
579 G418 antibiotic selection. Nuclear tagging with mVenus was performed by replacing mApple in
580 the strain above using CRISPR/Cas9. The mVenus fragment was amplified from plasmid pPH_086
581 using the same oPH_0944 and oPH_0945 primers and guideRNAs oPH_941 and oPH_942.

582 **4.3 Light stimulation experiments in 24-well-plates**

583 Overnight cultures were diluted 1:50 in fresh LoFlo-SC (synthetic complete media prepared with
584 "low fluorescence" yeast nitrogen base lacking folic acid and riboflavin; Formedium) to reduce

585 media fluorescence and grown to an optical density (OD_{600}) of 0.4–0.5. Individual day cultures of
586 optogenetic and reporter strains were washed once with 1 volume of LoFlo-SC media, resuspended
587 to an OD of 0.5, mixed at a 1:1 ratio, and placed in black glass-bottom 24-well plates (CellVis). Light
588 stimulation was performed in a custom-made light plate apparatus based on the design by
589 Gerhardt et al[27] equipped with a blue LED (λ=461 nm). The final volume in all experiments was 1
590 mL and the incubation time was 2 h. When opto-Bar1 was used as a test strain, α-factor (Sigma)
591 was added at a final concentration of 1 μM. A well containing only the reporter strain was routinely
592 included to calculate the basal GFP expression from the P_{C120} promoter. Light intensity calibration
593 of the apparatus was performed as reported before[27] using a power-meter and a custom 3D-printed
594 adaptor. Reporter gene expression was analyzed by flow cytometry immediately after sampling.

595 **4.4 Patterned light stimulation in Petri plates**

596 Day cultures in SD media containing all amino acids were inoculated at 4% *v*/*v* with an overnight
597 culture and grown until the OD_{600} was ~1.0The cultures were then centrifuged at 3500 rpm for 7
598 min, the supernatant removed, the pellets washed once in SD medium containing all amino acids,
599 and the optical density adjusted to OD_{600} =1.0. These suspensions were mixed at a 1:1 ratio and 150
600 μL was added to 6 mL of 0.5% agar ("top" agar, kept in a water bath at 55°C).

601 For the "velvet" version of the assay (**Figs. 3, S4, S5, S7**), the top agar was poured over Petri plates
602 containing solid SC-agar (1.5% agar; 20 mL total volume) supplemented with all amino acids.,
603 using a leveling surface. Plates were then sealed with parafilm, keeping the lids of the plates
604 slightly tilted. Blue light patterning was performed with a DMD projector (DLP® LightCrafter™
605 4500 TexasInstrument) placed inside an incubator (Memmert UF160); the projector projects light of

606 the desired shape and intensity over Petri plates placed over a black surface. After light stimulation,
607 the plates were replicated on SD plates lacking methionine and lysine using the sterile velvet
608 technique, incubated for at least 24 h at 30°C, and imaged using a multi-imager (Biorad) for colony
609 counting.

610 For the "direct" version of the assay (**Figs. 2, S4, S6**), agar cell suspension was poured over 20 mL
611 of 1.5% agar SD media with low lysin levels (0.005 g/L) and was directly recovered for imaging and
612 colony counting after at least 24 h of incubation (**Fig. S4**). The basis for this simpler version of the
613 assay relies on the following: because the *MAT*a and *MAT*α wild-type strains are auxotrophic for
614 methionine and lysine, respectively (**See Supplementary Table 1**), we expected haploid growth—
615 and presumably mating—to depend on supplementation of these amino acids. Consequently, a
616 low concentration of these amino acids would allow mating, but later only select for diploid growth
617 as these amino acids become exhausted. We note that the methionine levels in the 150 μL cell mixes
618 are enough to allow mating, as adding methionine did not increase diploid growth. On the
619 contrary, lysine levels were optimized to determine the final concentration used (levels higher than
620 0.005 g/L did not affect diploid growth). Calibration of the light intensity of the device was
621 performed by placing a power meter at the location of the agar surface.

622 **4.5 Half-domain gradient generation assay**

623 Rows of wells in glass-bottom 24-well plates (CellVis) were taped in the "row" direction following
624 available marks in the frame that coincide with the hemisphere of the wells. Longitudinal sections
625 of black tape were cut and the uncut side of the tape was gently positioned facing the hemisphere
626 of the wells. Overnight cultures were reinoculated at 2% *v*/*v* in YPD. These day cultures were grown

627 for 4 h, washed once in 4 mL of synthetic complete media with 2% glc (SC-GLC), and then
628 resuspended in 1 mL of the same media. The OD600 was determined in a cuvette benchtop
629 spectrophotometer using 100 μL of this culture and 900 μL of SD-glc. Cultures were diluted back
630 to OD_{600}=0.1 in a final volume of 5 mL **SC-glc**. Concanavalin A coating was performed as follows:
631 wells were exposed to 300 μL of 0.2 mg/mL Concanavalin A (ConA, Sigma; 1/10 dilution of a 2
632 mg/mL stock that was spun down to remove protein aggregates) for 6 minutes, then the solution
633 was removed from each well (using a the P1000 pipet and then a P200 for the remanent), washed
634 once with 300 μL of sterile water (water was removed in one strong inversion movement and not
635 pipetted out), then 300 μL of the appropriate cell suspension mixes were gently deposited
636 (consistently on the west side of each well) and allowed to settle gravitationally for 35 min. During
637 cell settlement, fresh 1.5% *w/v* low-melting point agarose (Sigma) was melted in SD-glc in a glass
638 beaker with constant and gentle magnetic stirring. Then, 200 μL of the hot (70°C) agarose solution
639 was taken out (reverse pipetted) with a 1000 μL (blue) tip, held for 10 seconds, and the solution
640 was gently (5 seconds to dispense 200 μL) was deposited in the bottom "west" position,
641 immediately followed by gently pipetting up and down (close to the middle high, also pointing in
642 the west direction). We set a light exposure time of 5 h, which allowed us to observe complete
643 development of the output curves. The total analyzed region was roughly 5.4 mm around the
644 border. Wells have a diameter of 1.554 cm and cells are embedded in a total volume of 0.5 cm^3 of
645 agarose.

646 **4.6 Flow cytometry**

647 Flow cytometry measurements were performed on an LSR II cytometer (Becton-Dickinson). GFP
648 fluorescence was measured with a 488 nm laser using BD FACS DIVA software (BD Biosciences).
649 First, cells were gated in an FSC-A/SSC- to exclude debris and doublets. GFP-positive cells (either
650 *MAT***a** or *MATα*, depending on the experiment) were gated manually using FlowJo (Becton-
651 Dickinson), and the mean fluorescence of this population was used for further analysis.

652 **4.7 Fluorescence microscopy**

653 Imaging of the half-domain assay was performed using a Leica DMi8 inverted microscope (Leica
654 Microsystems) equipped with a motorized stage and a 20x objective (N.A. 0.4) using *LasX* software
655 (Leica Microsystems) in multi-position mode. Fluorescence images were acquired using the 470/40
656 (Ex), 525/50 (EM) filter for GFP and the TXR filter 560/40 (EX), 630/75 (EM) filter for mApple
657 proteins, respectively. Imaging was also performed using an inverted Olympus IX81
658 epifluorescence microscope equipped with an "Xcite exacte" light source (I = 30%) and a filter cube
659 (EX) 514 nm/10 (EM) 545 nm/40 (49905 – ET) with a 1000 ms exposure time.

660 **4.8 Manual determination of cell-length**

661 As a proxy for the morphological response to pheromone we manually measured the cell-length
662 for cells in the half-domain experiment. In the opto-α experiment, a total of 6995 cells were
663 segmented, while in the oplto-Bar1 experiment the total was 8331 cells (a larger region was sampled
664 in this experiment). In the range considered for fits the total numbers analyzed correspond to 6686
665 and 6088 cells, respectively. Lengths were measured manually using the segmented line tool in Fiji
666 in single cells. On each identified cell, we measured its length by drawing a line along its longest

667 diameter. In elongated cells we draw their central longitudinal axis using as many points as needed
668 to maximize precision (elongated cells are curved). Although we counted mostly non-overlapping
669 cells, if a mild overlap existed, or the overlap produced clearly distinguishable boundaries, cells
670 were considered. Prezygotes (cells having a characteristic dumbbell shape, product of cell-cell
671 fusion events), were not considered in the analysis. In samples with large cell-clumps, we measured
672 regions close to empty spaces where little overlap existed. All cell segmentation data and original
673 images are available in Zenodo.

674 **4.9 Machine-learning based cell segmentation.**

675 Manual segmentation is very precise but laborious. We therefore complemented manual
676 segmentation analyses using machine-learning algorithms to obtain additional output data and
677 analyze control half-domain assay experiments. All datasets were pre-processed using rotation,
678 noise insertion, pixel intensity perturbation and translation. Cell segmentation was done on
679 brightfield images on the half-domain assay with two machine-learning algorithms using the U-
680 NET architecture. The first model was used to segment elongated cells and the second model to
681 segment round-shaped cells. The first model was trained on 21 images during 50 epochs. Its
682 accuracy was estimated at 0.97 and its recall at 0.89 (Fig. S11). The second model was trained on 10
683 images during 100 epochs and had an estimated accuracy of 0.91 and a recall of 0.73. All the training
684 was performed using a GPU NVIDIA Quadro RTX 4000 (7.5GB RAM memory).

685 After identifying cells as such, round-shaped ones were assigned the category of "receivers" or
686 "emitters" using fluorescence image information. Fluorescently labeled nuclei were also segmented
687 using machine learning. A unique model (same for mApple tagged nuclei and for GFP-tagged

688 nuclei) was trained (with GFP images but as well valid for RFP segmentation) over 30 epochs and
689 its accuracy was estimated to be 0.98.

690 In the opto-α generated gradient (Fig. 5), emitters carry a mApple (red) nuclear marker, whereas
691 receivers do not carry a nuclear marker. Cells identified as round with overlapping nuclear
692 segmentation are identified as emitters. In the opto-Bar1-generated gradient (Fig. 6), emitters carry
693 a GFP nuclear marker and were identified equivalently. Once all cells were segmented and the
694 receivers (elongated and round shapes) are identified from the emitters, a CSV file that contains
695 information about the identity of the segmented object (receiver or emitter), its position along the
696 experimental axis (in μm), area (in pixels), and the mean GFP intensity in the case of fluorescent
697 reporter receivers is produced (Fig. 5). For the latter, background subtraction was performed as
698 follows: a mask was produced that is the sum of the two segmentations from the models for round
699 and elongated shapes. The background then corresponds to the negative part of this mask in the
700 brightfield image. To calculate the orientation of elongated objects, an ellipse was fitted using
701 Python openCV ellipse fitting function and its angle (from 0° excluded to 180°) with respect to the
702 x-axis was extracted (Fig. S)

703 The data from the nuclei segmentation was used to count haploid and diploids (independently of
704 the shape analysis, which filters cells) as a measure of cell proliferation along the experimental
705 length in the half-domain assay (**Fig. S13**). Counting nuclei allowed us to count individual cells in
706 regions with clumps. It also allowed the easy identification of diploid cells events in the opto-bar1
707 experiment (**Fig. S13**).

708 **5.10 Quantification of the P_{FUS1} transcriptional response in single cells.**

709 Quantification of the P_{FUS1}-GFP response in the half domain assay was more precisely determined
710 segmenting images in the GFP channel, where false positives are minimal. First the images were
711 corrected for illumination inhomogeneities using the BaSiC package for imageJ[50]. The background
712 profile obtained using this tool was equivalent to the background extraction done by ML but
713 performs better in the smaller lengthscale (within-image inhomogeneities). The Cell Profiler
714 software (Broad Institute, Cambridge, MA) was used for the quantification of the transcriptional
715 response. The OTSU adaptive thresholding method was used for object identification in
716 fluorescence images. Cell clumps were discarded with an object-size threshold and a form-factor
717 filter to select rounder objects. Segmentation quality was inspected visually and empirically
718 optimized by changing filter and threshold values. All cell segmentation data and original images
719 are available in Zenodo.

720 **5.11 Data analysis**

721 ***Normalization and baseline subtraction of data.*** Cell elongation data as well as P_{FUS1} dependent
722 gene-expression at single cell level were provided as inputs to the downstream analysis. The
723 baseline of each dataset was identified as their mean value for distances to the border greater then
724 2700 μm on the right domain, at such distances the gradients are zero and the dataset can be
725 considered to having reached their asymptotic levels. After subtracting the baseline, the scaling
726 factor was obtained by measuring their mean value for distances to the border between 2000 and
727 1300 μm on the left domain, at such distances the gradients are zero and the datasets doesn't show
728 border effects due to reflective boundary conditions present for larger distances. Normalization
729 was obtained by dividing the baseline subtracted data by the scaling factor.

730 ***Fitting pheromone gradient generated by the spatial optogenetic induction of α-factor.*** Due to
731 difference in filtering, cell elongation data as well as P_{FUS1} dependent gene-expression at single cell
732 level had to be matched. This was done by binning the data in 100 μm wide bins and taking their
733 mean for the downstream analysis. Fitting was done using the least squares methods on both
734 datasets at the same time, to extract the parameters λ, C and n by fitting gene expression to $\hat{\theta}(x, \infty)$
735 with Hill coefficient equal to 1 and elongation to $\hat{\theta}(x, \infty)$ with free Hill coefficient n. Only integer
736 values between 1 and 7 were considered in the least squares minimization procedure for the n
737 parameter.

738 ***Estimation of α-factor maximum concentration on the left domain c_α^{max} in the spatial optogenetic***
739 ***induction of Bar1.*** Cell elongation data for the Bar1 induction experiment were binned and
740 normalized according to the same procedure used for the α-factor induction results. The
741 experimental data indicated a scaling factor for the Bar1 induction experiment equal to 5.75
742 compared to 7.20 measured in the α-factor induction experiment. Considering the measurement of
743 $C = 1.57\ \mathrm{EC}_{50}$ obtained in the α-factor induction experiment by fitting, we extracted the value of
744 c_α^{max} in the Bar1 induction experiment by numerically solving the following equation:

745 $$\frac{c_\alpha^{max3}}{1 + c_\alpha^{max3}} = \frac{5.75}{7.20} \cdot \frac{C^3}{1 + \mathrm{C}^3} \quad (7)$$

746 obtaining $c_\alpha^{max} = 1.20\ \mathrm{EC}_{50}$.

747 ***Determination of the half-maximal response in the spatial optogenetic induction of Bar1.*** In order
748 to measure the distance at which the half-maximal response in the Bar1 dataset occurs, we fitted

the following logistic function with one parameter, the half-maximal response λ_0, to the normalized baseline-subtracted data:

$$\frac{1}{1+\mathrm{e}^{\frac{n}{\lambda_\alpha}(x-\lambda_0)}}, \tag{8}$$

finding a value of $\lambda_0 = -1.16\,\lambda_\alpha$.

5.12 Numerical derivation of the half-maximal response in function of model parameters

In order to derive the steady state α-factor concentration profile $c_\alpha(x)$ from **Eq. 4**, we numerically solved the following differential equation:

$$\frac{{\lambda_\alpha}^2}{c_\alpha^{max}} c_\alpha''(x) - \frac{1}{c_\alpha^{max}} c_\alpha(x) - \frac{c_\alpha^{max} - c_\alpha^{min}}{c_\alpha^{max} c_\alpha^{min}} c_\beta(x) \cdot c_\alpha(x) + 1 = 0, \tag{8}$$

using the steady state analytical solution to **Eq. 4** for the shape of the Bar1 concentration profile:

$$c_\beta(x) = \begin{cases} \frac{1}{2}\mathrm{e}^{x/\lambda_\beta} & \text{for } x < 0, \\ \left(1 - \frac{1}{2}\mathrm{e}^{-x/\lambda_\beta}\right) & \text{for } x \geq 0, \end{cases} \tag{9}$$

and conveniently setting $\lambda_\alpha = 1$, such as to have all spatial variables (x and λ_β) expressed in λ_α units, and $c_\alpha^{max} = 1.20\ \mathrm{EC}_{50}$ to its experimentally determined value.

We then derived numerical solutions for $c_\alpha(x)$ using the Mathematica software package and the NDSolveValue function with Dirichlet boundary conditions c_α^{min} and c_α^{max}, with a large set of parameters c_α^{min} and λ_β distributed equally spaced on the logarithmic scale.

For each of these solutions, we obtained the corresponding $\theta(x, \infty)$ by combining them with the Hill function with coefficient $n = 3$. We further calculated the theoretical location of the half

maximal response λ_0 by taking the point where $\theta(x,\infty)$ crosses the value corresponding to the mean between its minimum and its maximum values over the full domain. The resulting table of λ_0 in function of $\lambda_\beta/\lambda_\alpha$ and $c_\alpha^{min}/c_\alpha^{max}$ was fed to the ListContourPlot function to plot **Fig 6C**. We used the same function to highlight the contour corresponding to the experimentally determined $\lambda_0 = -1.16\,\lambda_\alpha$ in dashed red, highlighting the set of values $\lambda_\beta/\lambda_\alpha$ and $c_\alpha^{min}/c_\alpha^{max}$ that are compatible with the experimental data.

Acknowledgments

The authors would like to thank their team members for their critical reading of this manuscript. This work was mainly supported by the European Research Council grant SmartCells (724813) and received additional support from grants ANR-11-LABX-0038, ANR-10-IDEX-0001-02, ANR-16-CE12-0025-01, and the QLife Institute ANR-17-CONV-0005

Author Contributions

AB conceived the research and contributed to all aspects of this work. MH, CE, SP, CC, and MLB contributed to optogenetic strain construction (MH, CE), experiments (MH, CE, CC), and setup of the optogenetic devices (MH, SP, MLB). LC contributed image analysis. VS contributed the modeling of the pheromone reaction-diffusion dynamics and their fit to experimental data. AB, VS, and PH interpreted the results. AB and PH designed the study. AB, VS and PH wrote the article.

Supplementary Information

Supplementary information contains 12 figures, the mathematical model, and two tables.

Bibliography

1. Simsek, M. F. & Özbudak, E. M. Patterning principles of morphogen gradients. *Open Biol.* **12**, 220224 (2022).

2. Stapornwongkul, K. S. & Vincent, J.-P. Generation of extracellular morphogen gradients: the case for diffusion. *Nat. Rev. Genet.* **22**, 393–411 (2021).

3. Mukherjee, S. & Bassler, B. L. Bacterial quorum sensing in complex and dynamically changing environments. *Nat. Rev. Microbiol.* **17**, 371–382 (2019).

4. van Gestel, J. *et al.* Short-range quorum sensing controls horizontal gene transfer at micron scale in bacterial communities. *Nat. Commun.* **12**, 2324 (2021).

5. Narla, A. V., Borenstein, D. B. & Wingreen, N. S. A biophysical limit for quorum sensing in biofilms. *Proc. Natl. Acad. Sci.* **118**, e2022818118 (2021).

6. Clark-Cotton, M. R., Jacobs, K. C. & Lew, D. J. Chemotropism and Cell-Cell Fusion in Fungi. *Microbiol. Mol. Biol. Rev.* **86**, e00165-21 (2022).

7. Ghose, D., Jacobs, K., Ramirez, S., Elston, T. & Lew, D. Chemotactic movement of a polarity site enables yeast cells to find their mates. *Proc Natl Acad Sci U A* **118**, (2021).

8. Bardwell, L. A walk-through of the yeast mating pheromone response pathway. *Peptides* **26**, 339–350 (2005).

802 9. Shellhammer, J. P. *et al.* Quantitative analysis of the yeast pheromone pathway. *Yeast* **36**,
803 495–518 (2019).
804 10. Yu, R. C. *et al.* Negative feedback that improves information transmission in yeast
805 signalling. *Nature* **456**, 755–61 (2008).
806 11. Muller, N. *et al.* A Predictive Model for Yeast Cell Polarization in Pheromone Gradients.
807 *PLOS Comput. Biol.* **12**, e1004795 (2016).
808 12. Malleshaiah, M. K., Shahrezaei, V., Swain, P. S. & Michnick, S. W. The scaffold protein Ste5
809 directly controls a switch-like mating decision in yeast. *Nature* **465**, 101–105 (2010).
810 13. Brett, M.-E., DeFlorio, R., Stone, D. E. & Eddington, D. T. A microfluidic device that forms
811 and redirects pheromone gradients to study chemotropism in yeast. *Lab on a Chip* vol. 12 3127
812 (2012).
813 14. Moore, T. I., Chou, C.-S., Nie, Q., Jeon, N. L. & Yi, T.-M. Robust spatial sensing of mating
814 pheromone gradients by yeast cells. *PLoS One* **3**, e3865 (2008).
815 15. Barkai, N., Rose, M. D. & Wingreen, N. S. Protease helps yeast find mating partners. *Nature*
816 **396**, 422–423 (1998).
817 16. Hanson, S. J. & Wolfe, K. H. An Evolutionary Perspective on Yeast Mating-Type Switching.
818 *Genetics* **206**, 9–32 (2017).
819 17. Jackson, C. L. & Hartwell, L. H. Courtship in S. cerevisiae: both cell types choose mating
820 partners by responding to the strongest pheromone signal. *Cell* **63**, 1039–1051 (1990).
821 18. Barkai, N., Rose, M. D. & Wingreen, N. S. Protease helps yeast find mating partners. *Nature*
822 **396**, 422–423 (1998).

823 19. Rappaport, N. & Barkai, N. Disentangling signaling gradients generated by equivalent
824 sources. *J. Biol. Phys.* **38**, 267–278 (2012).
825 20. Jin, M. *et al.* Yeast Dynamically Modify Their Environment to Achieve Better Mating
826 Efficiency. *Sci Signal* **4**, ra54–ra54 (2011).
827 21. Diener, C. *et al.* Yeast mating and image-based quantification of spatial pattern formation.
828 *PLoS Comput Biol* **10**, e1003690 (2014).
829 22. Vo, T., Shah, S. B., Choy, J. S. & Luo, X. Chemotropism among populations of yeast cells
830 with spatiotemporal resolution in a biofabricated microfluidic platform. *Biomicrofluidics* vol. 14
831 014108 (2020).
832 23. Hicks, J. B. & Herskowitz, I. Evidence for a new diffusible element of mating pheromones
833 in yeast. *Nature* **260**, 246–248 (1976).
834 24. Rojas, V. & Larrondo, L. F. Coupling Cell Communication and Optogenetics:
835 Implementation of a Light-Inducible Intercellular System in Yeast. *ACS Synth. Biol.* **12**, 71–82 (2022).
836 25. Motta-Mena, L. B. *et al.* An optogenetic gene expression system with rapid activation and
837 deactivation kinetics. *Nat. Chem. Biol.* **10**, 196–202 (2014).
838 26. Banderas, A., Koltai, M., Anders, A. & Sourjik, V. Sensory input attenuation allows
839 predictive sexual response in yeast. *Nat Commun* **7**, 12590 (2016).
840 27. Gerhardt, K. P. *et al.* An open-hardware platform for optogenetics and photobiology. *Sci*
841 *Rep* **6**, 35363 (2016).
842 28. Le Bec, M. *et al.* Optogenetic spatial patterning of cooperation in yeast populations. *Nat.*
843 *Commun.* **15**, 75 (2024).

844 29. Nath, R. Properties of Barrier, a novel Saccharomyces cerevisiae acid protease. *Biochimie* **75**,
845 467–472 (1993).
846 30. Kawada, D. *et al.* The yeast Arf-GAP Glo3p is required for the endocytic recycling of cell
847 surface proteins. *Biochim. Biophys. Acta* **1853**, 144–156 (2015).
848 31. Hilioti, Z. *et al.* Oscillatory phosphorylation of yeast Fus3 MAP kinase controls periodic
849 gene expression and morphogenesis. *Curr Biol* **18**, 1700–1706 (2008).
850 32. Arkowitz, R. a. Chemical gradients and chemotropism in yeast. *CSH Perspect Biol* **1**, a001958
851 (2009).
852 33. Paliwal, S. *et al.* MAPK-mediated bimodal gene expression and adaptive gradient sensing
853 in yeast. *Nature* **446**, 46–51 (2007).
854 34. Segall, J. E. Polarization of yeast cells in spatial gradients of alpha mating factor. *Proc. Natl.*
855 *Acad. Sci. U. S. A.* **90**, 8332–6 (1993).
856 35. Anders, A., Colin, R., Banderas, A. & Sourjik, V. Asymmetric mating behavior of isogamous
857 budding yeast. *Sci. Adv.* **7**, eabf8404 (2021).
858 36. Erdman, S. & Snyder, M. A filamentous growth response mediated by the yeast mating
859 pathway. *Genetics* **159**, 919–28 (2001).
860 37. Clark-Cotton, M. R. *et al.* Exploratory polarization facilitates mating partner selection in.
861 *Mol Biol Cell* **32**, 1048–1063 (2021).
862 38. Follette, P. J. & Arkowitz, R. A. Chemotropism During Yeast Mating. *Methods Mol. Biol.* **571**,
863 99–110 (2009).
864 39. Ismael, A. & Stone, D. E. Yeast chemotropism: A paradigm shift in chemical gradient
865 sensing. *Cellular Logistics* vol. 7 e1314237 (2017).

866 40. Stone, D. E. & Arkowitz, R. A. In Situ Assays of Chemotropism During Yeast Mating.
867 *Methods in Molecular Biology* 1–12 (2016).
868 41. Arkowitz, R. A. Responding to attraction: chemotaxis and chemotropism in Dictyostelium
869 and yeast. *Trends Cell Biol.* **9**, 20–27 (1999).
870 42. Knop, M. Evolution of the hemiascomycete yeasts: on life styles and the importance of
871 inbreeding. *BioEssays* **28**, 696–708 (2006).
872 43. Reuter, M., Bell, G. & Greig, D. Increased outbreeding in yeast in response to dispersal by
873 an insect vector. *Curr Biol* **17**, R81–R83 (2007).
874 44. Moukadiri, I., Jaafar, L. & Zueco, J. Identification of two mannoproteins released from cell
875 walls of a Saccharomyces cerevisiae mnn1 mnn9 double mutant by reducing agents. *J Bacteriol* **181**,
876 4741–4745 (1999).
877 45. Murphy, H. a & Zeyl, C. W. Yeast sex: surprisingly high rates of outcrossing between asci.
878 *PloS One* **5**, e10461 (2010).
879 46. Robinson, J. S., Klionsky, D. J., Banta, L. M. & Emr, S. D. Protein sorting in Saccharomyces
880 cerevisiae: isolation of mutants defective in the delivery and processing of multiple vacuolar
881 hydrolases. *Mol Cell Biol* **8**, 4936–4948 (1988).
882 47. Laughery, M. F. *et al.* New vectors for simple and streamlined CRISPR-Cas9 genome editing
883 in Saccharomyces cerevisiae. *Yeast Chichester Engl.* **32**, 711–720 (2015).
884 48. Rivera-Cancel, G., Motta-Mena, L. B. & Gardner, K. H. Identification of Natural and
885 Artificial DNA Substrates for Light-Activated LOV–HTH Transcription Factor EL222. *Biochemistry*
886 **51**, 10024–10034 (2012).

887 49. Zhao, E. M. *et al.* Optogenetic regulation of engineered cellular metabolism for microbial
888 chemical production. *Nature* **555**, 683–687 (2018).
889 50. Peng, T. *et al.* A BaSiC tool for background and shading correction of optical microscopy
890 images. *Nat. Commun.* **8**, 1–7 (2017).

891

892 # Figure 1

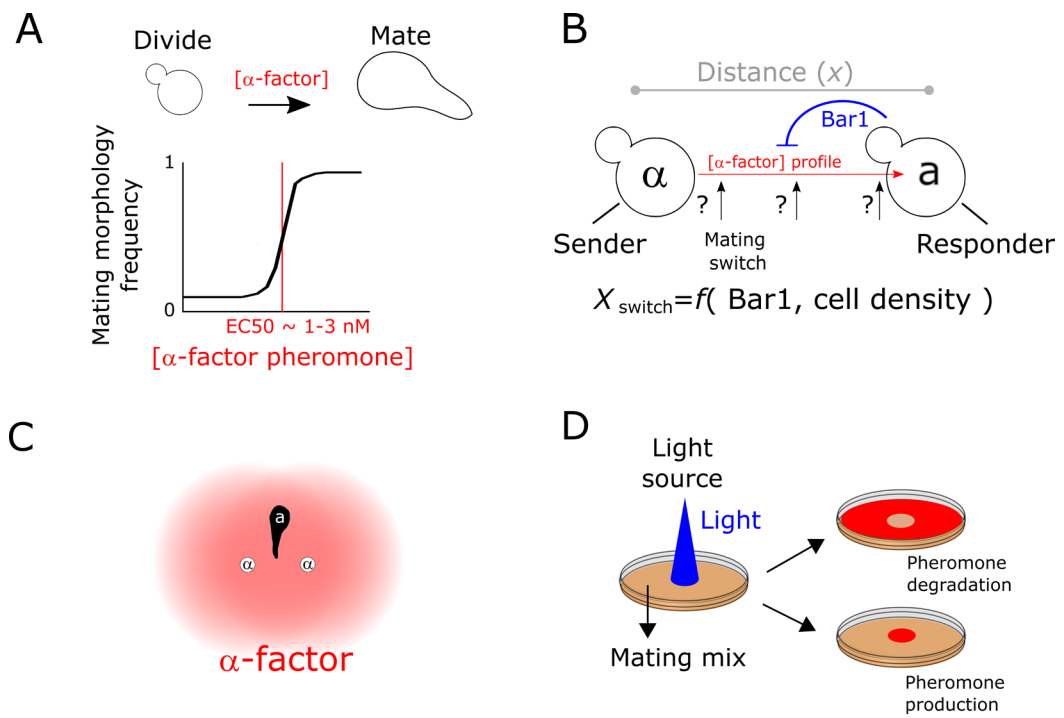

893

894 **Figure 1. Using optogenetics to interrogate the properties of cell-generated signaling gradients.**
895 **A.** The mating switch. Yeast cells switch from budding to mating morphologies when α-factor is
896 present (top). This dose-response is sharp and occurs in the nM range, close to the receptor Kd
897 across strains. **B.** When cells with opposite mating types are located at a distance, the generated α-
898 factor gradient (red arrow, indicating the direction of decay) has a strength (amplitude and
899 steepness) that defines where the concentration is sufficient for switching-on mating behavior. The
900 profile of the α-factor pheromone not only depends on the local density of emitters contributing to
901 the gradient, but also on the presence of the extracellular α-factor peptidase Bar1, and therefore on
902 the density of *MAT***a** cells. When Bar1 is absent or low, the position of the mating switch is expected

903 to happen at a distance. In contrast, if Bar1 is high, the mating switch is displaced towards the
904 source vicinity. **C**. Due to low Bar1 mediated degradation of α-factor when *MAT***a** populations have
905 low density, the α-factor gradients are expected to overlap and provide sufficient intensities to
906 trigger mating behavior at a distance, but at the cost of reduced precision due to "confusing" local
907 maxima. **D.** Optogenetic control of α-factor and Bar1 emission allows spatial control of these two
908 opposing activities. In the example shown, a Petri dish containing mating mixes is illuminated in
909 specific regions allowing us to stimulate production or degradation of the pheromone (red color),
910 depending on which genetic determinant is controlled.

Figure 2

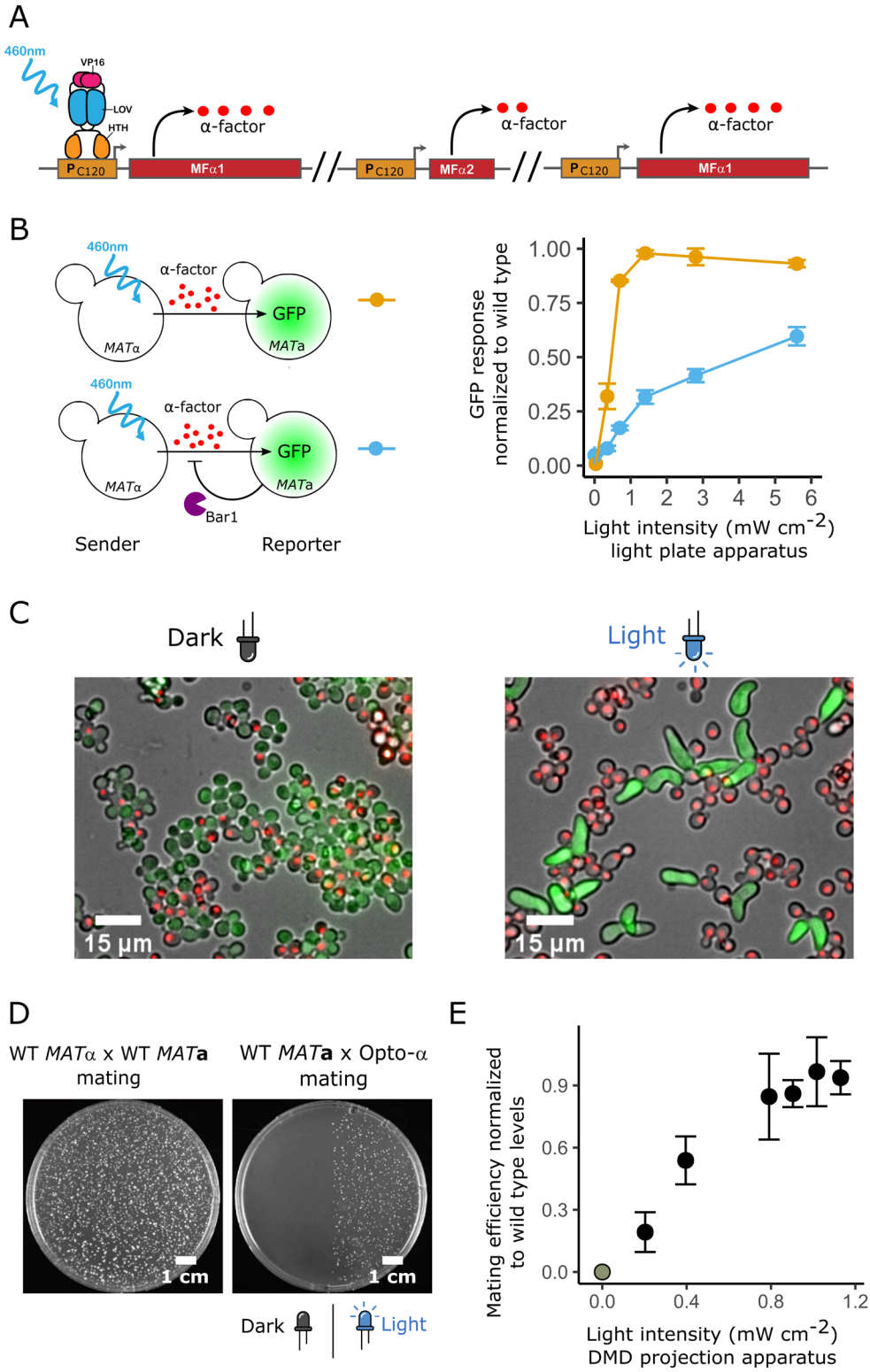
A
460nm
VP16
LOV
HTH
α-factor
α-factor
α-factor
P C120
MFα1
P C120
MFα2
P C120
MFα1
B
460nm
α-factor
GFP
MATα
MATa
460nm
α-factor
GFP
MATα
MATa
Bar1
Sender
Reporter
GFP response normalized to wild type
1.00
0.75
0.50
0.25
0.00
0 1 2 3 4 5 6
Light intensity (mW cm-2)
light plate apparatus
C
Dark
Light
15 µm
15 µm
D
WT MATα x WT MATa mating
WT MATa x Opto-α mating
1 cm
1 cm
Dark
Light
E
Mating efficiency normalized to wild type levels
0.9
0.6
0.3
0.0
0.0 0.4 0.8 1.2
Light intensity (mW cm-2)
DMD projection apparatus

913 **Figure 2. Optogenetic control of extracellular *α*-factor production allows tight spatial control of**
914 **mating.**

915 **A.** The light-responsive *α*-factor-producing "opto-*α*" strain was engineered by replacing the native
916 promoters of the two pheromone-coding genes in *MATα* (MF*α*1 and MF*α*2) with the P_{C120}
917 promoter, which is responsive to the light-activated LOV domain EL222 transcription factor, and
918 by later duplicating the MF*α*1 (which produces the highest amount of pheromone of the two genes)
919 light-responsive locus. **B.** The activity of the P_{FUS1} pheromone-responsive promoter in *MAT***a**
920 receivers in stirred mating reactions as a function of light intensity. In the assay, the opto-*α* strain
921 is co-incubated either with *bar1*Δ (top left) or a wild-type *MAT***a** (bottom left) P_{FUS1} GFP reporter
922 strain. After 2 h, the mixes are assessed by flow cytometry. As a control, the reporters are incubated
923 with wild-type *MATα*, and the baseline-subtracted relative response is calculated (right). Error bars
924 are the SD of n=3 biological replicates. **C.** Agarose-embedded *MAT***a** bar1Δ reporter strains (cells
925 carrying cytoplasmic GFP) co-incubated with opto-*α* cells (carrying a red nuclear signal expressed
926 by a mApple fluorescent protein) for 5 h under non-illuminated (left) and maximally illuminated
927 (5.8 mW/cm^2, right) conditions. **D, E.** Quantification of mating efficiency through light-controlled
928 pheromone production. Light induces cell-cell fusion in the optogenetic mating assay measured as
929 the appearance of diploid colonies only in illuminated regions (D). Quantification of the mating
930 efficiency at different light-doses. Efficiency is defined as relative to the activity of the wild-type
931 *MATα* strain (C). Error bars are the SD of n=3 biological replicates.

Figure 3

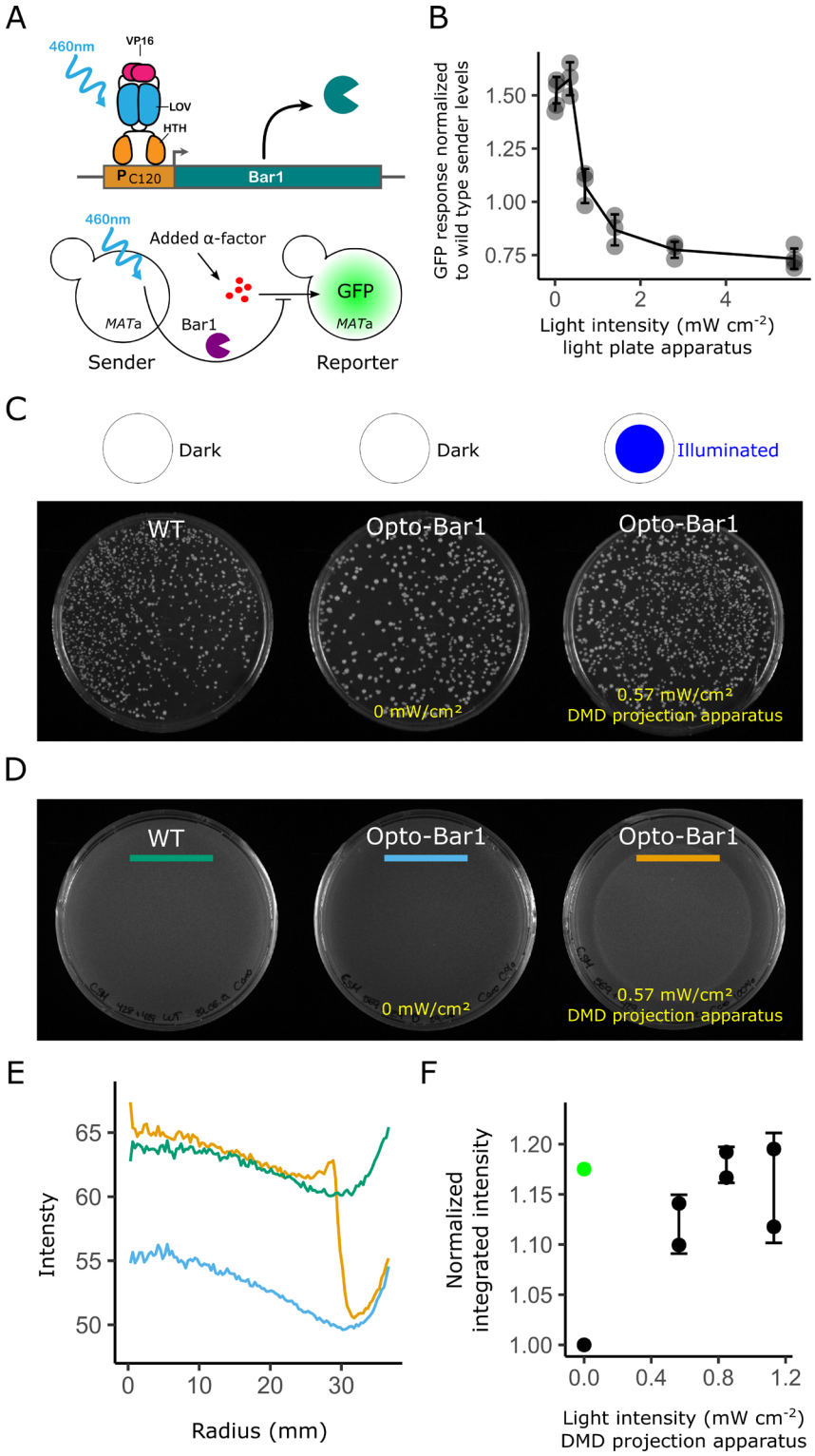
A
460nm
VP16
LOV
HTH
P C120
Bar1
460nm
Added α-factor
GFP
MATa
Bar1
MATa
Sender
Reporter
B
GFP response normalized to wild type sender levels
1.50
1.25
1.00
0.75
0
2
4
Light intensity (mW cm-2) light plate apparatus
C
Dark
Dark
Illuminated
WT
Opto-Bar1
Opto-Bar1
0 mW/cm²
0.57 mW/cm²
DMD projection apparatus
D
WT
Opto-Bar1
Opto-Bar1
0 mW/cm²
0.57 mW/cm²
DMD projection apparatus
E
Intensty
65
60
55
50
0
10
20
30
Radius (mm)
F
Normalized integrated intensity
1.20
1.15
1.10
1.05
1.00
0.0
0.4
0.8
1.2
Light intensity (mW cm-2) DMD projection apparatus

934 **Figure 3. Optogenetic control of extracellular signal degradation allows tight spatial control of**
935 **growth arrest.**

936 **A.** Promoter replacement in the Opto-Bar1 strain. EL222-mediated light-dependent expression of
937 the native *loci* encoding Bar1 in the *MAT***a** strain (top) and the pheromone activity assay, in which
938 exogenously added pheromone stimulates the sensitized GFP reporter strain (bottom). **B.** Resulting
939 light-dose response from the assay, measured by flow cytometry. The biological activity of the
940 pheromone is defined relative to the activity of the wild-type *MAT***a** strain. Error bars are the SD of
941 3 biological replicas**. C, D.** Diploid selective (C) and non-selective plates (D) showing mating
942 efficiency and growth, respectively in illuminated and dark regions. **E**. Quantification of avoidance
943 of cell cycle arrest in the Opto-Bar1 strain as a function of light intensity, based on the integrated
944 pixel intensity of a radial profile (traces shown correspond to the colored bars in D). **F.** Light-dose
945 dependency of cell cycle arrest in the Petri-dish assay. Growth is integrated over the entire plate
946 and normalized to the value of non-activated opto-Bar1 cells. Growth of the wild-type is shown as
947 a green dot. Error bars are the SD of two biological replicates.

948

Figure 4

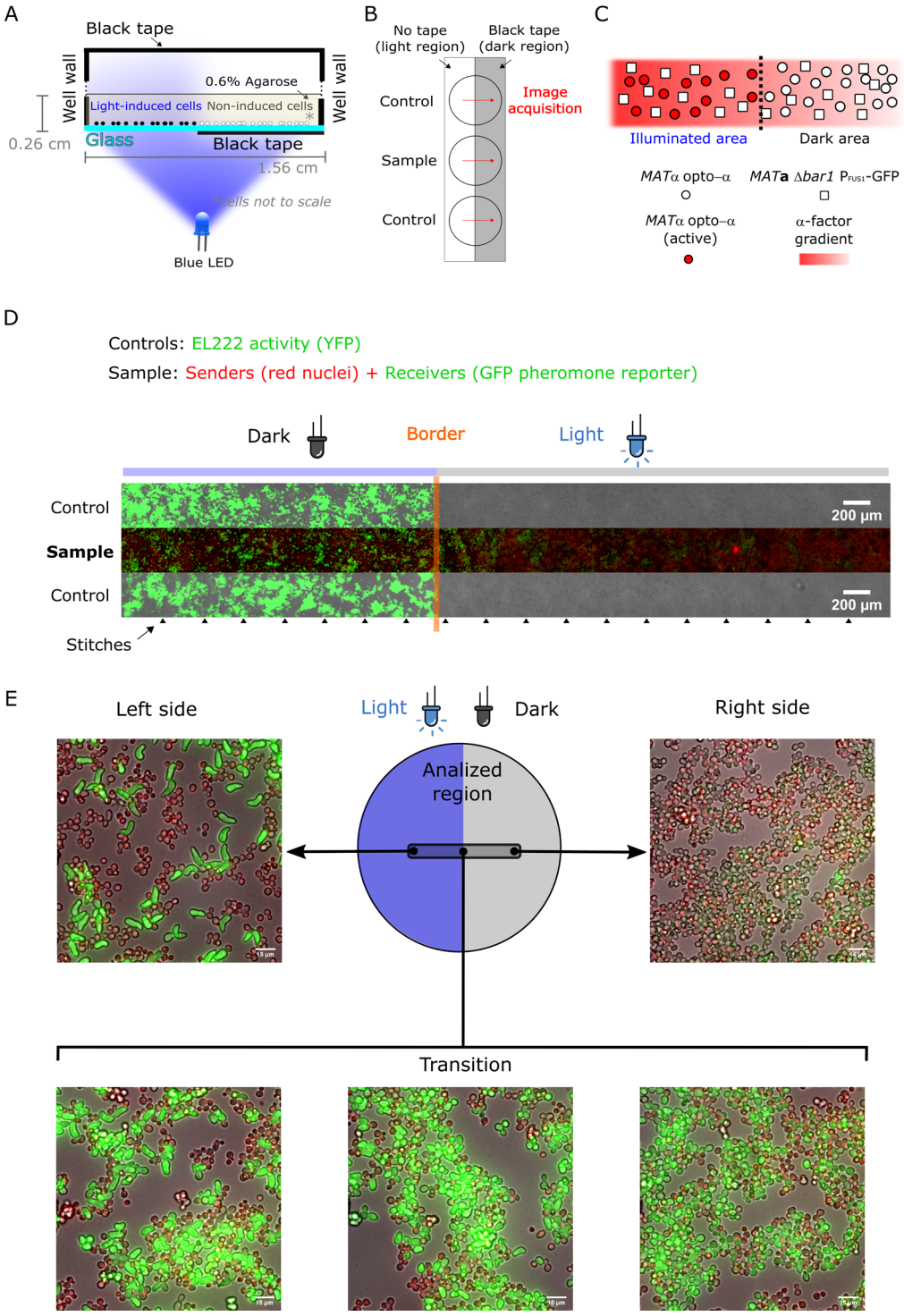
A
Black tape
Well wall
0.6% Agarose
Well wall
Light-induced cells
Non-induced cells
0.26 cm
Glass
Black tape
1.56 cm
*cells not to scale
Blue LED
B
No tape
(light region)
Black tape
(dark region)
Control
Image
acquisition
Sample
Control
C
Illuminated area
Dark area
MATα opto–α
MATa Δbar1 PFUS1-GFP
MATα opto–α
(active)
α-factor
gradient
D
Controls: EL222 activity (YFP)
Sample: Senders (red nuclei) + Receivers (GFP pheromone reporter)
Dark
Border
Light
Control
Sample
Control
200 µm
200 µm
Stitches
E
Left side
Light
Dark
Right side
Analized
region
Transition

951 **Figure 4. Optogenetic generation of pheromone gradients through the half-domain assay.**

952 **A.** Half-domain assay. Agarose-embedded cells are located at the bottom of the mini well and half
953 of the glass surface is illuminated to induce EL222-dependent expression. **B.** To determine the
954 position of the light border in samples along the acquisition path (red arrows), a control strain that
955 activates EL222-dependent fluorescent protein expression is run in parallel in adjacent wells. The
956 mean value of the border positions above and below the sample correspond to the position of the
957 light border in the sample. **C.** Schematic representation of the experiment, close to the light-dark
958 transition border. **D.** Microscopy image showing an overview of the mating reaction with the
959 controls for the border location (top and bottom row) displaying strong YFP fluorescence on each
960 side of the mating reaction (center row). Arrowheads at the bottom show where the image was
961 stitched together. In the sample mating reaction (center), opto-α has a red nuclear marker while
962 reporter *MAT***a** bar1delta expresses GFP when stimulated by pheromone. Samples were imaged
963 after 5 h of light exposure. **E.** Example fields along the experimental length showing the increased
964 abundance of elongated phenotypes and the increase in GFP levels in the illuminated region.

Figure 5

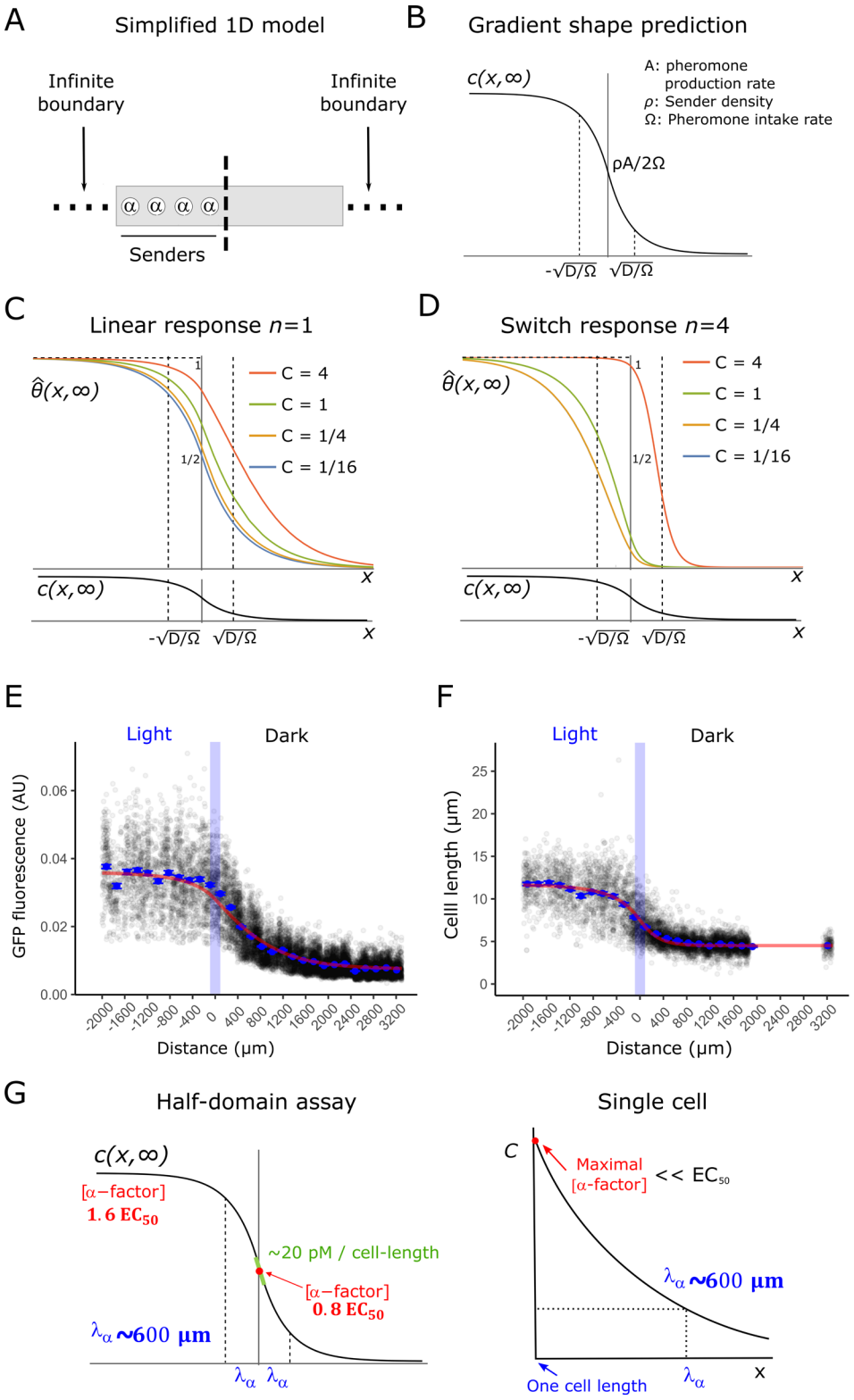
A
Simplified 1D model
Infinite boundary
Infinite boundary
α α α α
Senders
B
Gradient shape prediction
c(x,∞)
A: pheromone production rate
ρ: Sender density
Ω: Pheromone intake rate
ρA/2Ω
-√D/Ω √D/Ω
C
Linear response n=1
θ̂(x,∞)
C = 4
C = 1
C = 1/4
C = 1/16
1/2
c(x,∞)
x
-√D/Ω √D/Ω
D
Switch response n=4
θ̂(x,∞)
C = 4
C = 1
C = 1/4
C = 1/16
1/2
c(x,∞)
x
-√D/Ω √D/Ω
E
Light
Dark
GFP fluorescence (AU)
Distance (μm)
F
Light
Dark
Celll length (μm)
Distance (μm)
G
Half-domain assay
c(x,∞)
[α−factor]
1.6 EC50
~20 pM / cell-length
[α−factor]
0.8 EC50
λα ~600 μm
λα λα
Single cell
C
Maximal [α-factor] << EC50
λα ~600 μm
One cell length
λα
x

967 **Figure 5. Quantitative properties of optogenetically generated gradients recapitulate switch-like**
968 **and linear responses in *MAT*a cells. A.** Theoretical, one-dimensional arrangement of pheromone
969 sender cells on one half-domain of an infinite line and pheromone receivers in the other half-
970 domain. **B.** Concentration profile of α-factor at steady state (Eq. 2, See Supplementary Information,
971 section II). **C, D.** Normalized response of the receptor (Eq. 3 normalized by its maximal value, See
972 Supplementary Information, section II) for half-domain expression of α-factor, showing predictions
973 for responses using a Hill coefficient equal to n=1 (E panel) and n=4 (F panel). Hill coefficients
974 greater than one correspond to a shift in the response towards a higher concentration of α-factor
975 and a steeper response. **E.** Quantification of single-cell gene expression output and overlayed
976 model fit, with the Hill coefficient set to 1. **F.** Quantification of single-cell gene morphological
977 response and overlayed model fit, with a fitted Hill coefficient of 3. **G.** Population-level and single-
978 cell estimations of pheromone-profile parameters.
979

980 # Figure 6

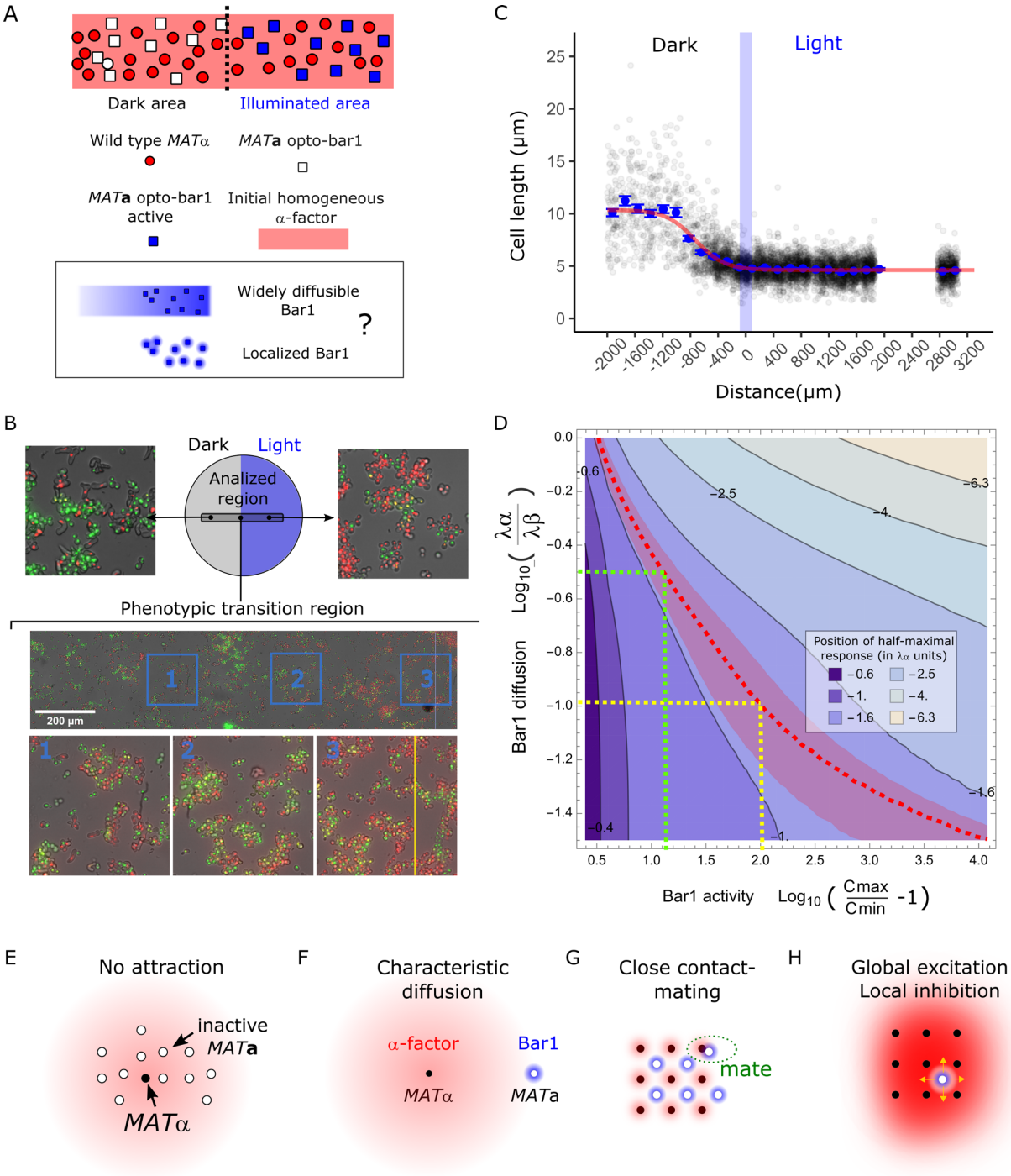

981

982 **Figure 6. Bar1-generated *α*-factor gradients reveal slow Bar1 diffusion. A.** Schematic
983 representation of the half-domain assay for opto-Bar1, close to the light-dark transition border.
984 Emitter cells produce alpha factor homogeneously. Light-induced Bar1 secretion occurs with

unknown spatial distributions (bottom box). **B.** Zoomed-out depiction of the half-domain assay for Bar1 production and microscopy imaging of Bar1 emitters (cells with red nuclei), receivers (cells with green nuclei), and newly formed diploids (cells with yellow nuclei). The yellow line represents the position of the left limit of the light-dark transition border. **C.** Quantification of the single-cell morphological response (cell length). The light border is represented by the blue vertical line corresponding to the border location determined with the controls run in parallel. The blue dots correspond to the mean value in each one of 30 bins and the error bar represents its standard error. The green dashed line represents the fitted "perfect sink" model; the orange line represents the 1-parameter fit of a shifted logistic function, used to determine the distance at which the half-maximum value of the response occurs (See Supplementary Information, Section III). The inset illustrates the prediction for the "perfect sink" model, showing the sharp concentration decay of Bar1 (top) used to obtain the generated α-factor profile (bottom). **D.** Contour plot showing the results of numerical simulations using the full mathematical model, showing the relation between diffusion of Bar1 relative to diffusion of α-factor and Bar1 activity for different α-factor profiles, characterized by the distance (in units of one α-factor decay length) that the half-maximal value of the induced response shows from the border (zero). The red dashed line highlights the isoline for the experimentally determined value of such a distance (See panel B). **E-H.** Basic properties of signal landscapes in yeast mating. Pheromone secretion by single cells does not provide positional information (E), as even sensitized partners (without expressing Bar1) sense a subthreshold concentration of pheromone., insufficient to trigger chemotropism. During mating, Bar1 has a lower steady-state decay length than α-factor (F). If the mating-type ratio is unbiased (G), Bar1 levels are sufficient to modify the overall pheromone profile. Consequently, cells do not elongate at a distance. Rather, short-range mechanisms[6] (focal pheromone emission, polarisome chemotaxis) allow mating in "touching" mates. If *MAT*α is abundant and *MAT***a** is not (H), Bar1 is insufficient to modify the global pheromone landscape but *MAT***a** will be also able to elongate (arrow) at a distance, because *MAT***a** is activated by pheromone concentrations from the contributions of several *MAT*α cells. Consequently, however, cells do not necessarily follow the right direction and elongate in random orientations.